

QC
807.5
.U6
W6
no.278
pt.1.c.2

NOAA Technical Memorandum ERL ETL-278



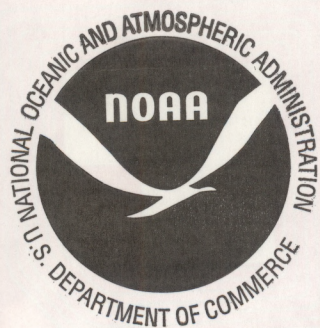
LABORATORY MODELING AND THEORETICAL STUDIES OF WAVE PROCESSES IN THE OCEAN

PART 1: EXPERIMENTAL DESIGN AND PROGRAM

L.A. Ostrovsky, Editor

Environmental Technology Laboratory
Boulder, Colorado
February 1997

noaa NATIONAL OCEANIC AND ATMOSPHERIC ADMINISTRATION / Environmental Research Laboratories



This memorandum corresponds (with minor changes) to the Experimental Design Report (Order Number 40RANR501545), prepared in accordance with the Memorandum of Understanding between the NOAA Environmental Technology Laboratory (ETL) and the Institute of Applied Physics (IAP) of Russian Academy of Sciences in Nizhny Novgorod, Russia. The work was performed in cooperation with ETL. It is supported by the joint NOAA/DOD Advanced Sensor Applications Program (ASAP).

Head of the Project: V. I. Talanov

Program Coordinator: L. A. Ostrovsky

Authors: S. D. Bogatyrev, V. V. Bakhanov, I. S. Dolina, S. A. Ermakov, E. A. Gromov., L. A. Ostrovsky, V. V. Papko, V. I. Talanov, V. V. Titov, Yu. I. Troitskaya, D. A. Zaborskikh

Translator: N. V. Rudik

NOAA Technical Memorandum ERL ETL-278

**LABORATORY MODELING AND THEORETICAL STUDIES OF WAVE PROCESSES
IN THE OCEAN**

PART 1: EXPERIMENTAL DESIGN AND PROGRAM

L.A. Ostrovsky, Editor

QC
807.5
146
W6
no. 278
pt. 1
c. 2

Environmental Technology Laboratory
Boulder, Colorado
February 1997



**UNITED STATES
DEPARTMENT OF COMMERCE**

**William M. Daley
Secretary**

**NATIONAL OCEANIC AND
ATMOSPHERIC ADMINISTRATION**

**D. JAMES BAKER
Under Secretary for Oceans
and Atmosphere/Administrator**

**Environmental Research
Laboratories**

**James L. Rasmussen
Director**

NOTICE

Mention of a commercial company or product does not constitute an endorsement by the NOAA Environmental Research Laboratories. Use of information from this publication concerning proprietary products or the test of such products for publicity or advertising purposes is not authorized.

For sale by the National Technical Information Service, 5285 Port Royal Road
Springfield, VA 22061

Contents

1	Introduction	1
2	Experimental Setups	2
2.1	Large Stratified Tank	2
2.1.1	Design	2
2.1.2	Formation and maintenance of temperature stratification	3
2.1.3	Experimental Equipment	4
2.1.4	Information-Measuring Complex	7
2.2	Small Stratified Tank	13
2.2.1	Design	13
2.2.2	Generation of temperature stratification	14
2.2.3	Experimental setup	15
2.3	Oval wind-wave tank	16
2.3.1	Design	16
2.3.2	Measuring equipment	17
3	Theoretical Models	18
3.1	Internal wave damping due to small-scale turbulence	18
3.2	Transformation of surface waves on a two-dimensional nonuniform current created by a moving dipole	21
3.3	Self-steepening of intense surface-wave packets on deep water	23
3.4	Cascade modulation of capillary-gravity ripples generated by surface gravity waves in an internal wave field.	26
3.5	Growth-rate modulation of short surface waves due to swell in the presence of turbulent wind	28
3.6	Generation of internal waves by stratified flow around obstacles	30
4	Planned Experiments and Preliminary Experimental Results	32
4.1	Internal-wave damping by small-scale turbulence	32
4.2	Surface-wave transformation by nonuniform flow around a moving sphere	33
4.3	Evolution of short trains of intense surface waves	35
4.4	Thermocline excitation by the short trains of surface waves	36
4.5	Surface-wave damping caused by turbulence	36

4.6	Nonlinear gravity-capillary waves and their modulation by internal waves	37
4.7	Nonlinear interactions of surface waves	38
4.8	Determination of surface wave-parameters with optical and radar techniques	39
5	Acknowledgment	42
6	References	42

Laboratory Modeling and Theoretical Studies of Wave Processes in the Ocean

Part 1: Experimental Design and Program

Edited by L. A. Ostrovsky

Abstract

Studies of the processes in the upper layer and on the surface of the ocean have been designed to increase understanding of internal and surface waves, turbulence, currents, and hydrodynamic motions generated by submerged bodies. The results will be helpful in developing remote sensing methods and devices for monitoring the ocean. Part 1 describes the unique laboratory facilities at the Institute of Applied Physics in Russia, including its thermostratified tanks and wind-wave tank; gives examples of theoretical models developed; outlines the laboratory experiments planned; and describes preliminary results confirming the validity of these experiments, such as observations of internal-wave damping by turbulence, surface-wave transformation by a flow around a moving sphere, and self-steepening of intensive surface-wave trains.

1 Introduction

Researchers at the Institute of Applied Physics (IAP) of the Russian Academy of Sciences in Nizhny Novgorod, Russia, have designed studies of wave processes in the upper ocean and on the ocean surface. The purpose of the studies is increased understanding of waves and turbulent processes in the ocean and their interactions, which will be helpful in developing remote sensing methods and devices for monitoring the ocean. Because of the great complexity of oceanic motions and multiple problems associated with the detailed *in situ* measurements, laboratory modeling of the corresponding processes has proved to be an effective tool for understanding the mechanisms of many oceanic motions and verifying theoretical models. The unique laboratory facilities at IAP, such as large and small thermostratified tanks and an

oval-shaped wind-wave tank, are ideal for many aspects of this study. In particular, the large tank admits an about 1:100 scale modeling of upper-ocean motions. Previous experiments with the use of these facilities have already demonstrated their high efficiency. We hope that the planned experiments, together with theoretical studies, will advance previous results of this group and others in this field, and will highlight the optimal ways for future field works.

The Memorandum is organized as follows. Section 2 gives a detailed description of the design, equipment, and working parameters of the three tanks mentioned above. In Section 2, theoretical results related to the processes to be studied are presented. Section 3 describes planned experiments and gives the results of preliminary experiments which demonstrate a few examples of the possibilities of the IAP laboratory tanks.

2 Experimental Setups

The hydrophysical laboratory of the IAP includes a large stratified tank; a smaller stratified tank (below: "small tank"); and an oval wind-wave tank. Their general functions and design are described below.

2.1 Large Stratified Tank

The overall view of the large stratified tank (LST) is shown in Fig. 1. It is a part of the hydrophysical laboratory (Fig. 2). The size of the tank - length 20m, width 4m, depth 2 m - was limited by the dimensions of the IAP building and by the position of its load-bearing structures.

2.1.1 Design

As shown in Figs 3 and 4, foundation (1) of the hydrochannel (2) of the tank is a concrete bowl whose bottom 1.2 m below ground level equal to 1.2 m. On the walls of the steel case of the tank, which have outer stiffening ribs, there are rails (8) that are mounted on controlled supports and set to an accuracy of 0.1 mm with respect to the water surface and to the diametral plane of the tank.

Inside the bowl at a height of 125 mm, we placed a second bottom (4) made of perforated steel sheets; it is connected at the ends to vertical walls

(9), that are welded in the sides at 200 mm from the main wall of the tank. Thus, a channel was created along the walls and the bottom that communicates with the bulk of the tank through ports in the second bottom.

Steel baffles (7) were installed along the walls at 175 mm from the wall and 700 mm below the upper edge of the tank. Inner surfaces of these baffles and the end baffles (12) were thermally insulated with polyurethane foam (10). Heat exchangers, each with an active area of 24 m^2 , were mounted on longitudinal baffles. Overflow ports (6) equipped with overflow controllers are located behind baffles in walls of the tank, 1850 mm from the bottom (2). Heat exchangers of the cold circuit (5), similar to the upper ones, were mounted below longitudinal baffle (7) on the tank walls.

The outer surfaces of the hydrochannel including the set of stiffening ribs and cold water pipelines, are completely thermally insulated (3).

2.1.2 Formation and maintenance of temperature stratification

To reduce the time of stratification formation, the water bulk below the temperature-difference layer (the thermocline) is cooled by replacing the initial water with water cooled by refrigerators with total capacity of 94 000 kcal/h. Note that to maintain the necessary stratification after its formation, one refrigerator of a capacity of 33000 kcal/h suffices. The cool water is pumped through the heat exchangers of the lower circuit. The scheme of the stratification generation and maintenance is shown in Fig. 5. Thus, while stratification is being formed, forced convection with high flow velocities occurs in the lower part of the hydrochannel; in operating regimes only free convection occurs.

The control station can combine the operation of the refrigerators and the heat station. For example, the control station enables water warmed at the heat station of the institute to pass through the heat exchangers of the upper circuit (with the refrigerators off) and to be cooled in a cooling tower when the water temperature is higher than the standard temperature. Institute through the heat exchangers of the upper circuit (the refrigerators are switched off), to cool this water by a cooling tower when the water temperature is higher than the standard one, to combine the operation of refrigerators and of the heat station, etc.

A typical profile of the stationary stratification and its evolution in time when refrigerators are switched off is shown in Fig. 6, and Fig. 7 shows the

stationary profile restored when the two large refrigerators are connected to heat exchangers. The Brunt-Vaisala frequency, the dispersion curves for the first two internal wave (IW) modes, and the vertical velocity profiles for the first and second IW modes are given in Figs. 8 through 11. Figure 12 shows the types of stratification possible in the large stratified tank.

2.1.3 Experimental Equipment

The experimental equipment of the tank includes:

- towing (self-propelled) trolley;
- surface-wave (SW) generator (wave maker) and IW generator;
- shear-flow inductor;
- rope-towing system;
- auxiliary equipment for calibration, servicing, and storage.

All the experimental equipment was designed at the IAP. The towing trolley is intended for the same service as that of the large test bases employed in shipbuilding, i.e., it is the base for mounting equipment to provide reliable information on the hydrodynamic characteristics of a tested (towed) model and on the hydrophysical parameters of stratified fluid in the tank (Fig. 13).

The trolley construction must be rigid, and it must ensure uniform motion in the measuring range. It is made of steel channels and box girders and has the form of a rectangular frame 3 m long and 4 m wide. The frame is carried by four pairs of wheels (10) placed on rails (2) which are set on adjustable supports (to an accuracy of 0.1 mm) on the sides of the tank (1). Transverse displacements are limited by vertical-axial rollers (not shown in Fig. 13) mounted in the same plane as wheel axes. Thus, sufficient rigidity of the trolley is provided.

Uniform motion is produced with high-momentum d. c. motor (7) mounted on the trolley and equipped with a built-in generator and a current sensor.

The designed velocity range of trolley motion (from 0.01 to 1.0 m/s) was achieved by means of three-speed reduction gear box (4), whose backlashes

slightly increase rotation irregularity. The total rotation irregularity is not larger than $\pm 2\%$.

A two-component dynamometer (6) was mounted on guides in the diametral plane inside the frame, enabling us to measure the lift and resistance forces affecting a towed body and their increments due to variations in trolley speed. The ranges of the measured forces are 0.0005-0.5 kG for resistance and 0.005-1.0 kG for lift.

A coordinate device (7) was placed in the part of the trolley window to the right of the dynamometer. Three horizontal guides (box girders) can move with respect to the diametral plane and can be accurately fixed within 0.1 mm. Carriages can be placed on these guides at any point with an error smaller than 0.5 mm. A streamlined vertical rod was fixed in the carriage having depth-discrete mounts for temperature and velocity sensors. The distance between mounts is 100 mm; the rod is adjusted for a height of 100 mm within an accuracy of 0.1 mm. The lower sensor is located 800 mm below water surface. Therefore, the coordinate unit provides a rather high accuracy of sensor positioning with respect to towed model (13) or to the diametral plane of the tank.

A similar coordinate device was mounted on the rear transverse beam of the trolley outside its window (11). To avoid shortening the operating length of trolley movement, the coordinate device can be automatically lifted upright as the trolley reaches the end of the tank. An instrumentation compartment (between the electric driver foundation and the dynamometer guides) incorporates the converters necessary to feed information to the sensors and to convert their signals for subsequent transmission to recorders outside the trolley.

A SW generator (8) with its own electric driver can be mounted in the front part of the trolley between its cantilevered longitudinal beams.

Above the generator is a platform (9) for additional instrumentation (e.g., lighting or filming equipment) or for a researcher.

A schematic diagram of the wave generator is given in Fig. 14. A cambered wing with a chord of 0.5 m and a span 3.6 m is rigidly fixed (across the tank between heating-circuit baffles) on a rigid platform that is equipped with an electric driver placed on depth-controlled mounts. A plate hinged to the electric driver eccentric performs angular oscillations at designated frequency and amplitude. The SW generator attached to the rear edge of the wing produces waves from 0.1 to 1.0 m long and from 5 to 60 mm high.

It can be fixed either at the front of the towing trolley or on the sides of the tank.

The IW generator schematically shown in Fig. 14b is a plate 0.6 m high by 3.6 m long (i.e., equal to the tank width between heat exchangers) that is capable of angular oscillations relative to the horizontal axis of symmetry. The ends of the rotation axis fit into the frame, which can be placed at any depth from 600 to 900 mm from the upper edge of the tank. The space between the movable plate and the water surface is separated with an immovable screen fixed in the frame. A similar screen, 300 mm high, is placed below. The clearance between the screen and the plate is about 10 mm. The plate is set in motion by a dc electric driver providing high stability and by a set of levers. A movable mount of the upper horizontal lever sets the rotation angle of the plate from 50 to 150 degrees. The oscillation period is 13 to 120 s. All basic constructions are from materials with the least thermal conduction.

The SW and IW generators are controlled from the central control board.

The shear-flow inductor (Fig. 15) was designed to produce uniform flow in a water layer (usually the upper layer) in the middle of the tank. The flow velocity is maintained in the range 1.0 to 10.0 cm/s. The inductor's overall dimensions are 19.75 m (length), 4.10 m (width), and 1.3 m (height); its mass is 1.280 kg.

The water-intake device and the nozzle are suspended on platforms (2) mounted on rails on the end walls of the tank; sections of water lines are rack-mounted on the tank bottom. Guide shields limiting the operating part of the tank can be fixed on these racks.

The water-intake set is an axial pump (4) located in the snail-shaped guide apparatus. The pump drains water from the operating part of the tank. In the water-intake device, the direction of the flow reverses, and the flow is forced (through air-tight rectangular cross-section channels) to the nozzle block where it reverses direction again. The flow enters the operating part of the tank through a grid that equalizes its velocity and through a honeycomb that aligns and regulates the flow. Horizontal flaps are placed at the nozzle output to change vertical angle of the flow.

On the platform of the water-intake set is motor (6) with an electric driver similar to that located on the wave generators and on the trolley. Torque is applied about both axial pumps by a chain gear.

As the operating flow temperature diminishes, heat losses can be compensated with electric heaters mounted in the upper cover of the water intake device. Any number of heaters can be automatically switched on and off in an emergency.

The rope-towing system (Fig. 16) is intended for free (without rod) towing of models of various submerged bodies in a stratified test tank. It is a flexible, 1-mm diameter steel cable (1) moving on guide rollers, two of which are fixed on rods (6) in the diametral plane at the opposite walls of the hydrochannel. The cable is set in motion with a dc motor (4), a reduction gear, and a pulling roller. Rods (6) enable us to vary the depth of the rollers within 300 mm from the middle position (600 mm from the upper edge of the tank), while cable tension and its change of operating (submerged) length are provided by a tensioning device (5).

The set is capable of towing various submerged bodies in the velocity range 0.01 to 0.5 m/s. The towing trolley equipped with sensors for measuring the dynamics of stratified fluid parameters can move with synchronous velocity or can be fixed in a certain region. An immovable guiding rope (not shown in Fig. 16) is mounted between rods (6).

Calibration and auxiliary equipment are not described, since their designs and functions are clear from the figures.

2.1.4 Information-Measuring Complex

The tank is equipped with modern instruments, metrologically certified and controlled.

The information-measuring complex can be conventionally divided into measuring equipment (sensors) and the automated equipment for accumulation, processing and recording of signals supplied by sensors. The measuring equipment was created in 1990 as a result of scientific research carried out in cooperation with the Mendeleev Metrological Institute (St. Petersburg). Experimental precision devices for measuring temperature and velocity of water flows were designed, fabricated, and studied. They include electric thermometers to measure background (average) values of water temperature and its variations, and flow-velocity meters. We also developed and investigated equipment for metrological support of water temperature measurements, including a standard electric thermometer and a small thermostat, both for calibration purposes.

Electric thermometers

Background values of the stratified liquid temperatures lie in the range 0 to 30°C with an error 0.05°C. They were measured with copper resistance thermometers switched into the unbalanced bridge circuit. Sixteen temperature sensors with the measuring range and accuracy previously mentioned have been fabricated; the output signal voltage range is ± 5 V; the excess hydrostatic pressure is 1 kG/cm². Background temperatures were measured by means of two eight-channel blocks of electric thermometers. Precision resistors and integrated circuits were employed. The stability of both blocks was checked over five months. Temperature sensors with a cable were placed in a thermostat to measure the insulation resistance of each channel once every two weeks and to determine the error for the total measurement range 0 to 30° C. The investigation confirmed that the precision characteristics of the electric thermometers that we designed comply with technical requirements.

The electric thermometer for temperature-pulsations measurements has four channels and four sensors. The pulsation measurement range is 0.003 to 10°C and the frequency range is from 0.01 to 40 Hz. It is a microthermocouple. Voltage proportional to temperature pulsations is transmitted through a three-wire circuit to the preliminary amplifier input, then to a normalizing amplifier, and finally to recording and processing equipment. The thermocouple is not capable of measuring constant temperatures and high-frequency temperature pulsations exceeding 80 Hz.

Flow velocity meters

We analyzed the requirements for measuring thermostratified fluid flow velocity and developed two types of flow-velocity meters (sensors):

- velocity meter of the hot-wire anemometer type, enabling us to measure average flow velocity and pulsation velocity simultaneously;
- average velocity meter which is essentially a hydrometric current meter with a conductivity converter.

The thermoanemometer sensor is a platinum-film temperature-sensitive resistor. Its output voltage, which is proportional to the heating current, characterizes the flow velocity. The sensor consists of two platinum-film

resistors R_p and R_k connected to the bridge forming two neighboring arms. The operating film R_p , which is sensitive to flow velocity, is heated more than the flow. The compensative film R_k , which is connected in series to the operating film, has practically the same temperature as the flow.

The device is intended to maintain the bridge in a nearly balanced state. Flow-velocity variations change the heated resistor R_p and, thus, affect the balance of the bridge. The voltage difference in a diagonally opposite pair of junctions is supplied to the amplifier, which alters its output current to change the temperature of R_p and, thus, to compensate variations caused by the flow; the bridge then returns to its initial stage. The resistance remains constant during the entire process. When the flow temperature changes, both the R_p and R_k films which are made of the same material, vary proportionally, and the voltage in diagonally opposite pairs of junctions of the bridge is invariable as is the heat current of the sensor. Since the dependence of the sensor heat current (or of the output voltage of the hot-wire anemometer, which is proportional to it) on the velocity is the basis of the device, the temperature error of the velocity measurement is practically eliminated (it does not exceed 0.015% of the average velocity). Velocity-pulsations measurement sensitivity depends mainly on the steepness of the calibration characteristic, which varies much less with temperature than the output voltage, and the resulting temperature error of velocity-pulsations measurement is about 0.1 to 0.2%.

The fabricated hot-wire anemometer sample was tested by means of a special hydrodynamic equipment in the Mendeleev Metrological Institute. The velocity-pulsations measurement error was less than 10%. The amplitude-frequency characteristic was flat within 2.2 dB in the range 1 to 100 Hz and 3 dB in the range 1 to 400 Hz.

Average velocity was measured with a digital hydrodynamic current meter. The rotational frequency of its rotor is proportional to the flow velocity. The rotational frequency is measured with a built-in electronic frequency meter.

The hydrometric current meter tests yielded the following results:

- average velocity measurement: 0.02-2 m/s;
- measurement error for velocities: lower than 0.1 m/s - not larger than 10%; 0.1-0.2 m/s - smaller than 6%; 0.2-2 m/s - not larger than 4%.

The meter is powered by 9-V battery. Its propeller diameter is 13.5 mm.

Metrological control devices for water temperature measurement A standard electric thermometer was designed to test and calibrate thermometers in thermostats and to calibration other measuring equipment in the tank without disassembling.

The standard thermometer was fabricated at the Mendeleev Metrological Institute and certified after one year of testing at IAP. Its basic metrological characteristics are: measurement range of 0 – 30°C; error not larger than 0.0025°C; time constant not larger than 0.3 s.

A small, precision water thermostat was designed for calibration of standard and operating thermometers; it has the following specifications:

- Reproducible temperatures range from 0.5 to 30°C. Spatial gradients of temperature in operating chamber are not more than 0.01°C/m.
- Temporal variations of temperature in the operating chamber 10 min after achieving the designated temperature are not more than 0.01°C.
- The rate of fluid heating by the main heater in the operating chamber is not less than 0.2°C/cm.
- The rate of fluid heating by the main and auxiliary heaters working together is not less than 0.6°C/min.
- The cooling rate is within 0.1 to 0.2°C/min. The small thermostat was also designed and fabricated in the Mendeleev Metrological Institute.

Capabilities

The automated measuring complex was designed for accumulation, recording, preliminary processing, and representation of signals supplied by various sensors. The designed technological and experimental equipment and measuring devices enable us to measure the following in the stratified tank:

- stratification profile;
- IW and SW parameters;

- hydrodynamic characteristics of various bodies submerged in the stratified fluid;
- shear-flow characteristics.

The automated complex is designed for

- accumulation and recording of data in real time;
- primary processing and visualization during the course of an experiment;
- control of complex system functions and experimental procedures;
- reduction of processing, storage, and recording times.

The hardware components of the system, shown in the block diagram of Fig. 17, can be divided in two subsystems according to the arrangement of controlled sensor groups of the complex: stationary and movable.

The stationary subsystem is intended for

- data accumulation from corresponding sensor groups;
- control of experimental programs;
- preliminary data processing;
- data storage;
- loading and starting programs in the movable subsystem;
- visualization on the graphics monitor and on the system terminal;
- printing or plotting data;
- data communication to the IBM PC for further processing.

The stationary subsystem components are shown in Fig. 17. A separate subsystem with similar functions (a microcomputer, CAMAC crate and modules, and a distribution box) is placed on the towed trolley.

The accumulation and control system in the CAMAC standard was developed together with the automation system.

In conclusion, the automated complex described above is sufficient to ensure the performance of a basic set of experiments in the tank. The complex will be improved and modernized to fulfill the requirements of new research problems.

Planned development of the measuring complex

To investigate the spatial distribution of the SW characteristics for wavelengths from millimeters to decimeters, we planned to create a complex of remote optical and radio equipment in the large tank. The proposed equipment will also enable us to increase the efficiency of experiments on the SW variability parameters under the action of nonuniform currents and internal waves.

The optical remote-sensing-system includes a gradient light source, which can illuminate a 1.5 m^2 surface, at the tank bottom, and a nadir-aimed optical sensor mounted on a moving trolley 2 m above the surface. Two types of optical receivers are to be used: optical spectrum analyzers working in incoherent light and a TV camera. The spectrum analyzers use optical modulators with variable transparency described in [1]. The water-surface image is modulated by means of an optical modulator and is accumulated at the detector diode. This setup enables us to record, in real time, the variability of SW spectral density at fixed frequencies over a wide frequency band without preliminary recording of the surface image. A number of such devices with various ranges of fixed spatial frequency numbers, recorded SW propagation directions, and the times for obtaining statistically reliable estimates of spectra [2] have been developed at IAP, which enabled us to use a most adequate set for each experiment. These devices have already been successfully employed by us under field conditions and, after slight modernization, they can be used in laboratory experiments.

The second type of the optical receiver is a TV camera. Utilizing the available CCD-30 LP camera, the miroVIDEO DC1 clip-image-input board, FAST SCSI host adapter DEC-880B, and hard disk FUJINSU M2694ESA, we shall assemble a system for direct recording of surface-water TV images on a PC. The developed processing programs will enable us to correct the TV image and the spectral and correlation processing. The gradient illumination source is being enhanced now.

The activities devoted to remote radar sensing include

- Creation of an X-band scatterometer, enabling one to measure the backscattering cross section and the Doppler spectrum of the signal. It will be used with a Gann diode, a power amplifier, and frequency radiation modulation. As a receiving antenna, either a horn with the directivity diagram 15 degrees wide, or a parabolic antenna with the directivity diagram of 3 degrees will be used. The developed scatterometer will have a higher radiation power than current devices and be able to measure the Doppler spectrum and the backscattering cross section under field conditions over a wide range of observation angles: from nadir to grazing angles of several degrees.
- Modernization of the available Ka-band scatterometer for recording the Doppler spectrum. The Ka-band scatterometer is made by using a Gann diode with frequency modulation. It has been successfully employed in the JUSREX-92 experiment. The scatterometer modernization is aimed at measuring the Doppler spectrum in the tank when this spectrum is shifted to some carrier frequency.

2.2 Small Stratified Tank

While the large tank (LST) was being designed, the small stratified tank (SST) was constructed to principally model new designs and to develop methods for scale modeling of the hydrophysical processes of the upper ocean. This goal has been achieved when the LST was built (1992); however, the small tank is also being used now, since it is proper to test many experimental problems with a small model before large-scale tests are started.

2.2.1 Design

The SST shown in Fig. 18 is a steel rectangular basin (5 m long, 1.6 m wide, 1.2 m deep) with outer stiffening ribs. The outer surface, including the bottom, is covered with thermally insulating plastic foam sheets 60 mm thick. Pipelines, which connect the refrigerating plant to heat exchangers, are welded in the end wall of the tank. In the first design heat exchangers were a set of vertical pipes 10 mm in diameter, connected with longitudinal collectors. The thermocline depth was varied by using an intermediate section connected to either a warm or a cold circuit. However, it was no easy

matter to fabricate this SST and to repair it leaked. In the final design, the heat exchangers were duraluminium pipes of constant 50-mm cross section, as shown in Fig. 19, hinged on the inner surface of walls. The lower ones were connected to the refrigerating plant; the upper one, to the cooling system of refrigerators.

2.2.2 Generation of temperature stratification

The refrigerating plant consists of two refrigerators feeding a common evaporator. Machines of this type are designed to be used in stationary chambers; then are equipped with dry ribbed evaporators (4 for each machine). In our setup, all eight evaporators are enclosed in a leak-tight case through which antifreeze is pumped; the antifreeze then runs to the lower heat exchangers of the tank. In this design, their total cooling capacity amounts to 4000 kcal/h.

The stratification profile obtained is shown in Fig. 20 (curve 3). Curves 1 and 2 in the same figure are profiles from the first design of heat exchangers. Note that the maximum gradient is practically independent of the heat-exchanger design, whereas the time of establishing the stationary mode in the second design is about 1.5 times less (6 to 7 hours) for the 10° C initial temperature of water. Curve 4 shows the temperature profile 8 h after the refrigerator was turned off; in this case, a thermocline with a rather high gradient seen to be conserved. Therefore, experiments of 3 to 4 h duration 3-4 hours can be performed with the refrigerators turned off, and the stratification profile will remain practically the same.

An example of the temperature distribution, the conventional density and the squared Brunt-Vaisala frequency for the second design of heat exchangers is shown in Fig. 21. These characteristics were employed to calculate the dispersion curves of the first three modes of IWs, their phase velocities, and vertical velocity versus depth at various frequencies (these curves are not given in the report). The maximum Brunt - Vaisala frequency N_{\max} equals 0.4 rad/sec in the model (the corresponding buoyancy period $T_s = 15$ s); the maximum phase velocity of IW of the first mode is $V_1 = 5.2$ cm/s, of the second mode, $V_2 = 1.2$ cm/s; and of the third mode, $V_3 = 0.75$ cm/s. The scale similarity factor k for the model can be assumed to be equal to 100, which under natural conditions corresponds to the typical temperature gradient 1°C/m at the depth of the thermocline, ≈ 40 m. After rescaling

the IW characteristics, we obtain values quite realistic for the ocean. Principal schemes of scale modeling and stratification generation in the SST are presented in Figs. 22 and 23.

2.2.3 Experimental setup

The SST is a model of the LST and, thus, all experimental equipment was first modeled and tested in it. The SST has a towing device, SW and IW generators, shear-flow inductor, and an information-measuring system.

The towing device is a type of monorail. A high-power flange beam is placed in the diametral plane of the tank at a half-meter from the water surface; on it rails are mounted and adjusted in height and width to an inaccuracy of 0.1 mm. A carriage on four rollers moves along these guides, driven by a winch with a dc motor. A dynamometer with a towing rod can be mounted on the carriage, enabling one to measure the wave drag affecting the bodies moving in the thermocline region. The carriage is used for assembling other measuring equipment.

Different designs of SW and IW generators have been investigated including those described in the section 2.1 (LST). The IW generator used now is a semicylinder, 160 mm in diameter 1400 mm long, oscillating along a vertical wall. The oscillations occur in the thermocline region; their frequency and amplitude are controlled. The SW generator is a semisubmerged cylinder 80 mm in diameter, oscillating with an assigned frequency and amplitude along the same vertical wall. The wall and the IW generator are made of thermal insulators.

The design of the flow inductor is the same as that described for the LST and approximately a 1/5 scale of the latter.

The information-measuring system, developed at IAP RAS enables one to carry out the following in the SST:

- measure a stratification profile;
- determine parameters of IWs and SWs;
- measure semiempirical characteristics of models of various bodies towed in the stratified fluid;
- measure characteristics of shear flows.

2.3 Oval wind-wave tank

The oval wind-wave tank (Fig. 24) was constructed at IAP to investigate the mechanisms of generation, dissipation, and interaction of short wind waves, as well as the interaction between SWs and IWs, including:

- analysis of the wind-wave spectrum and its dependence on fetch;
- investigation of short-wave damping by surface-active films;
- study of capillary ripple generation by nonlinear gravity waves;
- analysis of the kinematic and cascade mechanisms of gravity-capillary wave modulation under the IW action for one-dimensional wave propagation.

To solve these problems the oval wind-wave tank is equipped with sets of IW and SW mechanic generators, a blower for making wind waves, a device for providing salt stratification, and a measuring complex.

2.3.1 Design

The oval wind-wave tank is a closed channel with two straight-line operating sections 2.4 m long and two semicircular sections with a radius of 1.9 m. The continuation of one of the operating sections is a 1.2 m long auxiliary section containing an IW generator and connected to the blower for generating an air current. The total height of the tank is 0.59 m, the width is 0.29 m, and the maximum water depth in the hydrochannel is 0.3 m. In one of the operating sections there is a trolley about 0.8 m above the tank cover. It can move above the tank along the rails and can be equipped with remote (optical or radar) measuring equipment.

The stratification is created in the tank by using a salt solution fed through a set of hoses from a 2- m^3 reservoir placed above the tank. The salt solution is delivered to the tank through special ports in the bottom at a controlled speed. As a rule, the experiments were performed with a two-layer fluid, although continuous stratification can also be created. Typical density jumps in the stratification models employed are within 0.05 to 0.1 g/cm³. Acrylic plastic windows (45 cm × 40 cm) were installed in the side walls of the operating sections of the tank (4 per each side), and 4 windows (14.5

cm \times 14.5 cm) were installed in the bottom of the operating sections. The IW generator is a vertical blade 23 cm high, oscillating around the middle horizontal axis and driven by a dc motor. The oscillation amplitude of the blade is controlled by an eccentric; the frequency by the motor voltage. The characteristic IW periods are from 3 to 10 s, and typical IW wavelengths can vary in the range 15 cm to 2 m, depending on the frequency and the stratification parameters; IW amplitudes usually do not exceed 2 to 2.5 cm.

The SW generator is a vertically oscillating quarter cylinder driven by a dc motor. The amplitude and frequency of the oscillations are controlled like those of the IW generator. The characteristic frequency range of the SW generator is 2 to 8 Hz; the maximum oscillation amplitude is 1 cm. The SW generator can be placed at any point in the tank.

The wind flow is generated by a blower connected to the tank with a canvas hose. The blower has a restraint enabling one to control the average wind speed within 0 to 5 m/s.

2.3.2 Measuring equipment

Surface waves are measured by using a wire gauge, a laser slopometer, and a laser meter of the surface curvature. The wire gauge is designed for measuring surface oscillations at frequencies less than 20 to 30 Hz. The laser slopometer includes a laser mounted under the tank bottom. The laser beam, which is directed upwards, is recorded by a system placed above the tank. The receiver is a photosensitive strip, so that the slopometer measures wave slopes in only one direction; respectively, the beam is transformed into a knife beam with a cylindrical drum lens. The slopometer enables measurement of slopes of waves with frequencies of 100 Hz and less. The measurement of SW curvature is based on focusing the laser beam passing through the curved water surface. To avoid ambiguity of curvature measurements when a beam passes through IW crests and troughs, preliminary defocusing of a beam is used. The curvature measurements are within 1 cm^{-1} and less.

The interface oscillations due to IW are measured with a wire gauge similar to the SW wave-recording gauge (see ref. 3).

Another method of measuring the spatial SW spectrum is being developed now; it uses an optical spectrum analyzer (OSA) and an artificial gradient illuminator. The OSA has been successfully used to make full-scale measurements of wind-wave spectra (see, e.g., ref. 4). It is expected that the

application of OSA under the laboratory conditions will enable measurements of wave spectra in the wavelength range from 5 to 10 cm to a few millimeters.

3 Theoretical Models

3.1 Internal wave damping due to small-scale turbulence

Various mechanisms of energy exchange between internal gravity waves and turbulence in the ocean and atmosphere are known. Internal waves may amplify (or generate) turbulence as a result of their instability or breakdown [5- 7]. On the other hand, the turbulence produced by mechanisms independent of wave presence may act on IWs and lead to their damping. The possibility of IW damping due to small-scale turbulence has been demonstrated in a laboratory experiment performed by Phillips [7, 8], and the first theoretical estimates of IW damping due to turbulent viscosity have been reported by LeBlond [9]. Later, Ostrovsky and co-workers [10, 11] showed that turbulent diffusion can lead to strong damping of long waves, probably up to the inertial range. However, a common disadvantage of these studies was that some important ocean features were neglected, and practically no quantitative experiments were performed.

Recently we developed a more general theory and considered a model describing IW damping due to small-scale turbulence in stratified fluids, with parameters typical of the real upper ocean (stratification, distribution of turbulent energy and shear flow over depth) [12].

The theoretical model of IW propagation in a turbulent, stratified fluid is based on a two-dimensional set of equations of the semiempirical turbulence theory:

$$\begin{aligned}\vec{U}_t + \left(\vec{U} \nabla \right) \vec{U} &= \frac{\partial}{\partial x_i} \left(K_i \frac{\partial \vec{U}}{\partial x_i} \right) - \nabla \frac{P}{\rho_0} + \vec{g} \frac{\rho}{\rho_0}; \\ \rho_t + \left(\vec{U} \nabla \right) \rho &= \frac{\partial}{\partial x_j} \left(K_{\rho i} \frac{\partial \rho}{\partial x_i} \right); \\ \nabla \vec{U} &= 0;\end{aligned}$$

$$b_t + (\vec{U} \nabla) b = \frac{\partial}{\partial x_i} \left(K_{bi} \frac{\partial b}{\partial x_i} \right) + K_j \left(\frac{\partial \vec{U}_i}{\partial x_j} + \frac{\partial \vec{U}_j}{\partial x_i} \right) \frac{\partial \vec{U}_i}{\partial x_j} + \quad (1)$$

$$K_{\rho z} \frac{g \partial \rho}{\rho_0 \partial z} - K_j \frac{b c^4}{l_j^2};$$

with a simple closure scheme for transfer coefficients:

$$K_j = l_j \sqrt{b}; K_{\rho j} = K_j \kappa_\rho; K_{bj} = K_j \kappa_b; c^4 \approx 0.05,$$

where \vec{U} is the average velocity vector, ρ and P are, respectively, the density and pressure averaged over turbulent pulsations, \vec{g} in the gravity acceleration vector, b is the kinetic energy density of turbulent pulsations, l_j are turbulence scales, and $\kappa_\rho \approx 0.1, \kappa_b \approx 0.7$ are empirical constants [11]. The set of equations was solved by the perturbation method [13] with the assumption of a small spatial damping of IW per wavelength. The solution is sought as follows:

$$\vec{U} = \vec{U}_0 + \vec{U}_1 + \dots; \varpi = \varpi_0 + \varpi_1 + \dots; \rho = \rho_0 + \rho_1 + \dots; b = b_0 + b_1 + \dots,$$

where ϖ is the wave frequency at a given wave number k ; the index "0" refers to the assigned stationary distributions of undisturbed values in depth, and the index "1" refers to the perturbations created by the IW. Based on the assumption of small turbulence effect at a wavelength scale, a solution was obtained in [12] that gives an expression for the damping rate (the decrement) for each IW mode. Here, we present a particular case of this formula that is valid when shear flow is absent:

$$\varpi_1 = -i \left[\int_{-H}^0 2N^2 W_0^2 dz \right]^{-1} \left\{ k^2 \int_{-H}^0 K_{\rho x} N^2 W_0^2 dz \right.$$

$$\left. + \frac{\varpi_0^2}{k^2} \int_{-H}^0 W_0 \left[\frac{d^2}{dz^2} \left(K_z \frac{d^2 W_0}{dz^2} \right) + K_z k^4 W_0 - 2k^2 \frac{d}{dz} \left(K_z \frac{dW_0}{dz} \right) \right] dz \right\} \quad (2)$$

where H is the total depth, $W_0(z)$ is the vertical velocity of IWs and $\varpi_0(k)$ is the unperturbed dispersion relation for an internal wave mode, obtained

by solving the well-known boundary-value problem [5]:

$$\frac{d^2 W_0}{dz^2} + k^2 \left(\frac{N^2}{\varpi_0^2} - 1 \right) \varpi_0 = 0 \quad (3)$$

with the boundary conditions $W_0(0) = 0$ and $W_0(-H) = 0$. Calculations for the realistic ocean conditions were performed in ref. 12. The distributions of temperature, shear flow, and turbulent-energy density over depth corresponded to experimental data given in ref. 15. The first three modes were considered in detail.

The calculations showed that the wave-damping rate is proportional to the squared wave number ($\varpi_0 \propto k^2$ as conventionally accepted in literature) only for rather short waves and it remains finite as the wavelength increases. Note that the maximum damping rate differs from that for a medium with constant viscosity. The long-wave decrement does not depend on the wavelength but depends only on the mode number. Let us give estimates: for the buoyancy frequency typical of the main thermocline of the ocean, $N \propto 10^{-3} \text{s}^{-1}$, the kinetic energy density of turbulent pulsations is $B \approx 1 \text{cm}^2/\text{s}^2$, and in the absence of a shear flow for the wavelengths $\lambda > 4-6 \text{ km}$, the decrement for the first mode is $\varpi_1 \cong 10^{-6} \text{s}^{-1}$, whereas that for the second one is $\varpi_1 \cong 10^{-5} \text{s}^{-1}$. This means that for a 10-km wave the damping distances are 100 and 10 wavelengths for the first and third modes, respectively.

Some theoretical estimates can be checked experimentally in laboratory. In particular, in the large tank for a typical buoyancy frequency of 0.3 rad/s, the kinetic-energy density of pulsations in a turbulent jet of 0.05 cm/s, a turbulence scale of 10 cm, and the characteristic IW frequency 0.15 rad/s, one can expect the damping rate to equal 0.01 s^{-1} . This corresponds to the time of wave damping at a distance of about 4 m, which can be measured under the laboratory conditions.

For a realistic case of two weakly coupled waveguides (modeling the seasonal and main thermoclines), the effect of anomalously weak damping of IW at higher modes (beginning with the second one) has been discovered. The shear-flow effect on IW damping (in the absence of critical layers) was also investigated. Estimates show that the damping due to turbulence of the upper ocean should be an effective energy sink for relatively long IWs.

3.2 Transformation of surface waves on a two-dimensional nonuniform current created by a moving dipole

Increased interest in the study of the influence of inhomogeneous currents on SW characteristics is closely related to the development of facilities of remote diagnostics of subsurface processes, such as nonuniform currents, internal waves, rings, as well as perturbations created by submerged objects. All theoretical studies known to us deal with the transformation of SW in idealized models in which the current velocity depends on only one horizontal coordinate: $\mathbf{u} = U(y)\vec{x}_0$ or $U(x)\vec{x}_0$ [15-18]. Variations of the SW characteristics are usually analyzed by the ray method: the paths of the wave packets and variations of the SW amplitudes along them are calculated.

We investigated the influence of a weak *two-dimensional* current $\mathbf{u}(x, y)$ on gravity waves in deep water. A model equation for an SW amplitude has been obtained and solved numerically. Here we shall illustrate the results by considering amplitude variations of a wave propagating against a current perturbed by a dipole flow, which can be produced by a moving object.

The most essential changes in the SW parameters occur, when the projection of the wave group velocity onto the flow direction is close in absolute value and opposite in sign to the current velocity (group synchronism or blocking effect, see ref. 18). Therefore, to provide efficient action of a weak two-dimensional nonuniform current on SWs, they should be (in the comoving reference frame) decelerated by the main counterrunning current. This situation can occur in the ocean when SWs propagate counter to a current (for example, a tidal flow), that is perturbed by an underwater obstacle, such as a bottom elevation.

Let us assume that the characteristic scale of the current nonuniformities (horizontal and vertical) is much larger than the wavelength and, thus, larger than the scale of the wave-field variation in depth. Hence, by assuming the current velocity to be the function of only the horizontal coordinates, the dispersion relation for surface waves in deep water is

$$\left[\omega - \vec{k} \left(-V\vec{x}_0 + \vec{u}(x, y, t) \right) \right]^2 = g \left| \vec{k} \right|, \quad (4)$$

where \vec{k} is the wave vector of surface waves, V is the velocity of an unperturbed current directed counter to the axis x , $\vec{u}(x, y, t)$ is the current velocity

perturbation near the surface in a limited region, and ω is the wave frequency in the immovable (with respect to bottom) reference frame. Now we introduce the dimensionless variables $\bar{k} = \vec{k} / k_*$, $\bar{\omega} = \omega / k_* V$, and $\bar{\beta} = \vec{u} / V$, where $k_* = g/4V^2$ is the wave number of the wave, the group velocity of which equals V . The parameters of the unperturbed surface wave climbing the nonuniform current region are designated as $\bar{\omega}_0$, \bar{k}_{x0} and \bar{k}_{y0} , and variations of these parameters as a result of the current action are Ω , κ_x , and κ_y . We choose the positive branch of the dispersion relation in Eq.(4), and then obtain

$$\Omega + \bar{\omega}_0 = -\bar{k}_{x0} - \kappa_x + \bar{k}_{x0} \beta_x + \kappa_x \beta_x + \bar{k}_{y0} \beta_y + 2 \left[\left(\bar{k}_{x0} + \kappa_x \right)^2 + \left(\bar{k}_{y0} + \kappa_y \right)^2 \right]^{1/4} \quad (5)$$

Using the Eq. (5), one can derive a model equation for the wave amplitude. For this purpose we introduce the operators:

$$\frac{\partial}{\partial t} = i\Omega, \quad \frac{\partial}{\partial \bar{x}} = -i\kappa_x, \quad \frac{\partial}{\partial \bar{y}} = -i\kappa_y,$$

$$[(-\Delta^{1/4} J)](\bar{x}, \bar{y}) = \frac{1}{2\pi} \int e^{i(\kappa'_x \bar{x} + \kappa'_y \bar{y})} \left[\left(\bar{k}_{x0} - \kappa'_x \right)^2 + \left(\bar{k}_{y0} - \kappa'_y \right)^2 \right]^{1/4} \bar{J}(\kappa'_x, \kappa'_y) d\kappa'_x d\kappa'_y.$$

Here $\bar{J}(\kappa'_x, \kappa'_y)$ is the Fourier transform of the function J

$$\bar{J}(\kappa'_x, \kappa'_y) = \frac{1}{2\pi} \int e^{-i(\kappa'_x \bar{x} + \kappa'_y \bar{y})} J(\bar{x}, \bar{y}) d\bar{x} d\bar{y},$$

where $\bar{t} = tk_* V$, $\bar{x} = xk_*$, and $\bar{y} = yk_*$ are the dimensionless time and coordinates. For the complex amplitude of the SW a we obtain

$$\frac{\partial a}{\partial t} = 2i(-\Delta)^{1/4} a + (1 - \beta_x) \frac{\partial a}{\partial x} - \beta_y \frac{\partial a}{\partial y} + i \left[(-1 + \beta_x) \bar{k}_{x0} + \beta_y \bar{k}_{y0} - \bar{\omega}_0 \right] a.$$

This equation was solved numerically in a square with a grid of 256×256 points. The time evolution of an initially uniform wave field at a current

perturbation arising at a time $t = 0$ was investigated. Calculated results of the $|a|^2$ value variations on a current of a dipole located at a depth h are given in Fig. 25; for example

$$\beta_x = c \frac{2 \overset{-2}{x} - \overset{-2}{y} - \overset{-2}{h}}{\left(\overset{-2}{x} + \overset{-2}{y} + \overset{-2}{h} \right)^{3/2}}, \beta_y = 3c \frac{\overset{-2}{x}\overset{-2}{y}}{\left(\overset{-2}{x} + \overset{-2}{y} + \overset{-2}{h} \right)^{3/2}}, \quad (6)$$

where c is the dipole power and $h = hk_*$. The characteristic size of the region occupied by the nonuniform current is 20, whereas the size of the calculated region is 256×256 . The size of the region where the transformation is essential is considerably larger than the nonuniform current scales. In the course of time, a quasi-steady nonuniform pattern of perturbations forms in the vicinity of the scattering region. The perturbed wave pattern is anisotropic; in particular, isolated directions appear in which the field variations are concentrated.

When the unperturbed wave parameters (k_{x0} and k_{y0}) vary, the wave field pattern transforms markedly. Thus, when the projection of the group velocity of the unperturbed wave onto the x axis is larger than V , the main variations of the wave field occur at $x > 0$. When an incident surface wave has the component $k_{y0} > 0$, the variations will take place primarily at $y > 0$ and vice versa.

The specific features of the field of scattered SWs mentioned above were qualitatively explained by analyzing the dispersion relation of waves on the current.

Further we plan to analyze the SW transformation in two-dimensional currents by taking into account the wave nonlinearity.

3.3 Self-steepening of intense surface-wave packets on deep water

The nonlinear evolution of the nonlinear SW packets was analyzed theoretically and experimentally by Benjamin and Feir [19, 20], Yuen and Lake [21], and others. A most prominent result of these studies was that the finite-amplitude Stokes waves turn out to be unstable with respect to slow

modulation of their amplitude, and that stationary wave packets (envelope solitons) can exist for such waves. Theoretical analysis of such processes is usually performed in frames of the nonlinear Schrödinger equation (NSE) for a slowly varying complex amplitude ψ of the wave [21] (in dimensionless variables):

$$2i\frac{\partial\psi}{\partial t} + \frac{\partial^2\psi}{\partial\eta^2} + |\psi|^2\psi = 0, \quad (7)$$

where $\eta = x - V_g^l t$, V_g^l is the group velocity of the linear wave at the carrier frequency. An analysis of the next-order effects occurring outside the frames of this equation is associated with rather cumbersome calculations [22] that impeded their thorough analysis.

At the same time, such extensions are rather interesting. Actually, as in the field of electrodynamics and nonlinear optics [23-25], the dependence of the wave-group velocity on its intensity (nonlinear dispersion) may result in new effects that are absent in Eq. (7); in particular, in the wave "self-steepening" and, in the presence of nonlinear relaxation, in the formation of envelope shock waves in the form of stable "jumps" of the wave amplitude and frequency.

A typical model equation taking this possibility into account is a modified NSE equation with nonlinear dispersion:

$$2i\left(\frac{\partial\psi}{\partial t} + \frac{\partial\psi}{\partial\eta}|\psi|^2\right) + \frac{\partial^2\psi}{\partial\eta^2} + |\psi|^2\psi = 0. \quad (8)$$

This equation is not invariant with respect to the substitution of $-\eta$ for η . It follows from Eq. (8) that the groups with larger amplitudes move with larger group velocities. As a result, the leading front of an initially symmetrical wave packet will steepen up to its "breaking," when additional dispersive or dissipative mechanisms which define the evolution of steep fronts, enter into the process.

Let us consider the evolution of a one-dimensional quasi-harmonic packet of intense deep-water waves by taking into account the dependence of the group velocity on the intensity: $V_g^{nl}(|a|^2)$. In this case the equation for the amplitude $a(\xi, t)$ of the water surface displacement, $a \exp[i(\omega_0 t - k_0 x)]$, has a form similar to that of Eq. (8):

$$2i \left(\frac{\partial a}{\partial t} + \Delta V_g^{nl} \frac{\partial a}{\partial t} \right) + \frac{\omega_0}{4k_0^2} \frac{\partial^2 a}{\partial \eta^2} + \omega_0 k_0^2 |a|^2 a = 0, \quad (9)$$

where ω_0 and k_0 are the frequency and wave number related by the linear dispersion relation for the SW: $\omega_0 = \sqrt{gk_0}$; $V_g^l = \partial\omega_0/\partial k_0 = \frac{1}{2} \left(\frac{g}{k} \right)^{1/2}$, ΔV_g^{nl} is the group-velocity deviation from its linear value V_g^l equal to

$$\Delta V_g^{nl}(|a|) = 3V_g^l k_0^2 |a|^2 \quad (10)$$

This relationship is obtained from the nonlinear dispersion equation for intense gravity waves on deep water [26]. Because $\Delta V_g^{nl} > 0$, it again follows that groups with larger amplitudes move with larger group velocities, so that the leading front of the initially symmetrical packet will steepen. The characteristic time of breaking t^* can be estimated as the time of the packet maximum displacement ($|a| = a_m$) by its halfwidth:

$$t^* \simeq \frac{\Delta}{2\Delta V_g^{nl}} \simeq \frac{\Delta}{6V_g^l k_0^2 a_m^2}$$

The corresponding distance x^* amounts to $t^* V_g^l = \Delta/(6k_0^2 a_m^2)$. In particular, for a SW packet with a carrier frequency of $\nu = 1.6$ Hz ($\lambda = 58.5$ cm), a length $\Delta \simeq 140$ cm, an amplitude $a_m \simeq 3$ cm, ($k_0 a_m = 1/3$), and a symmetric envelope, we have $L^* \simeq 2$ m. Numerical simulation of Eq. (9) was performed in dimensionless variables:

$$\tau = \frac{t}{T}, \xi = \frac{\eta}{l}, \psi = \frac{a}{a_m}, \quad (11)$$

with the constants defined by: $\omega_0 T = 9$, $k_0 l = 3/2$, $(k_0 a_m) = 1/3$.

In these variables we obtain Eq. (8). As an initial condition for this equation, we took a symmetric wave packet with the envelope described by an even function without phase modulation:

$$\psi(\eta, 0) = \frac{\psi_0}{ch(2\xi/\delta)} \quad (12)$$

with the values of the dimensionless parameters $\psi_0 = 1$ and $\delta = 10$, which in dimensional variables correspond to the SW-packet amplitude $a_m = 1/3k_0$, and to its length $\Delta = 3\lambda\delta/4\pi = 140$ cm (the case mentioned just above).

The profiles of the modulus of the packet envelope, $|\psi(\xi)|$, for various times are given in Fig. 26. The plot (a) corresponds to the initial instant of time, $\tau = 0$, (b) to $\tau = 7$, (c) to $\tau = 14$, and (d) to $\tau = 21$. The distance L from the wave generator is related to dimensionless time τ by $L = 0.415 \tau$. Hence, the time instants in Fig. 26 correspond to distances $L = 0$, $L = 2.9$ m, $L = 5.8$ m, and $L = 8.7$ m, respectively. Note that first the leading front of the packet steepens, then the packet breaks into two and more pulses of various amplitudes [Figs. 26 (c) and 26 (d)].

3.4 Cascade modulation of capillary-gravity ripples generated by surface gravity waves in an internal wave field.

Steep gravity waves with wavelengths from about 3 to 30 cm and rather large amplitudes are known to generate near their crests short capillary-gravity waves (so-called *parasitic ripples*) propagating along the frontal slopes of steep waves (see, e. g., refs 27 and 28). These ripples' origins are connected with the nonlinear process of generation of higher harmonics by a gravity wave of finite amplitude. These harmonics move with the phase velocity of the fundamental gravity wave. Since the phase velocity of gravity waves is higher than the minimum phase velocity of gravity-capillary waves, some high-order harmonics can nearly satisfy the dispersion relation in the capillary-gravity wavelength range for resonant excitation of the ripples in the form of capillary-gravity wave trains moving along the steep gravity-wave profile. From laboratory experiments [28, 29], as well as from numerical modeling [30], it was concluded that the parasitic ripple steepness depends very strongly on the local curvature of the gravity-wave crests, and it does not depend on the total wavelength of the latter. Moreover, the ripples exist only when the curvature of the steep wave crest exceeds some threshold value. The amplitude of the parasitic wave trains achieves its maximum near the steep gravity-wave crests and decreases along its slope. The maximum of the parasitic ripple wavelengths is about 0.6 cm.

The presence of internal waves results in the parasitic ripple modulation. In the simplest model, the ripple steepness can be assumed to be a function of the local crest curvature of basic SWs and independent of the latter's wavelength. Let us assume the short gravity-wave curvature K to be mod-

ulated by a large-scale current due to an IW. This leads to the modulation of the parasitic ripple steepness S . It is easy to show that the modulation coefficients of the parasitic ripples M and of the short gravity wave m are proportional to each other:

$$M = Am \quad (13)$$

Here $A = d(\ln S)/d(\ln K)$ is an "amplification factor" of the parasitic ripple modulation. For a threshold-like dependence of the ripple steepness on the steep wave curvature when the short-wave curvature is close to a critical value, corresponding to the ripple excitation, we have $A \gg 1$. Therefore, we can expect that under some conditions the parasitic ripple modulation can essentially exceed the short gravity-wave modulation. Since the parasitic ripples are indirectly affected by IWs owing to the modulation of short gravity waves, this modulation mechanism can be considered to be a cascade-type modulation. Cascade modulation depends on the fundamental wave amplitude and is expected to have a maximum near its threshold value.

Our field experiments indicate that such cascade modulation may be significant when centimeter-long ripples are transformed by IWs. As an example, Fig. 27 exhibits synchronous records of SW spectral-density variations, the wavelengths being 35 cm (b) and 1.6 cm (c and d), and of sound-scattering layers produced by IW trains (e), see ref. 31. The specific features of wind-wave anomalies occurring in the field of a short IW train are seen in the figure: the variations in the spectral density of ripples before the IW train: the so-called precursor of anomalies, and the scales of ripple spectral-density variation much less than the IW period. These peculiarities are due to the complex motion of decimeter-range SW packets acting on the variable current produced by IWs on the surface; they may be explained in the frames of the kinematic model [32.] In the centimeter-long SW range, the "memory time" of wave packets is inessential. Thus, the record of these ripple peculiarities indicates a cascade character of IW action on the ripples: the current generated on the surface by IWs transforms the decimeter-long waves, and they, in turn, stimulate the ripple transformation. Note that the correlation coefficient of the spectral-density variations of the centimeter-long ripples [Fig. 27(c)] with the corresponding value for the decimeter-long waves [Fig. 27(b)] calculated in the region of well-expressed surface anomalies produced by IWs amounts to 0.6, whereas the correlation with the function describ-

ing the sound-scattering layer oscillations is only 0.3. As was demonstrated during the JUSREX-92 field experiment, when the modulation of decimeter-long SW is recorded, the centimeter-long ripples with close propagation are usually modulated as well. directions. Manifestations of the cascade modulation mechanism in the field conditions are mentioned in ref. 33, in which the results of the first laboratory experiment on parasitic ripple modulations in the IW field are also given.

Further development of the theory of cascade modulation of parasitic ripples implies a description of ripple modulation for the case of random gravity-wind waves, in particular, by use the empirical model of the short wind-wave spectrum recently suggested in ref. 34.

3.5 Growth-rate modulation of short surface waves due to swell in the presence of turbulent wind

Mechanisms of short SW modulation in the presence of long waves have been intensely studied in recent decades [35]. Interest in this problem is primarily due to the necessity of constructing a theory of radar images of long waves, since short SWs are radar-signal scatterers. This problem is often characterized by the strong differences in temporal and spatial scales of long and short waves: their wavelengths are, respectively, from tens to few hundred of meters and from centimeters to few decimeters; their periods are from a few to ten and more seconds and fractions of a second; and their phase velocities are tens of meters per second and tens of centimeters per second. Besides, under typical ocean conditions, the long-wave steepness is much less than the critical value of 0.142π .

Two mechanisms leading to short-wave modulation by long waves are known. The first one is due to the generation of harmonics close to the crests of steep gravity waves [27, 30]. It is efficient only when the long-wave steepness is close to the limiting one. The second mechanism is due to the transformation of short waves on a long-wave current [16, 17, 36, 37].

Smith and Valenzuela and Wright [35, 38] have shown that essential modulation of the short-wave spectrum may be caused by the modulation of their growth rate (the increment) in the presence of a long wave. This problem was considered only phenomenologically; in particular, the oscillating component of the increment was not calculated. We consider the mechanisms of short-

wave-increment modulation in the presence of a long wave. It is evident, that the wind increment is determined by the structure of the air flow above the wave. When a long surface wave with wave number k , phase velocity c , and the elevation amplitude a is propagating in water, a variable current occurs on the surface. A long-wave-scale current is also induced in the air with the same spatial and temporal periods, and, as a result, the short-wave increment is modulated. When the region of energy exchange between the wave and the flow lies within the viscous sublayer of the logarithmic boundary layer where the profile $U(y)$ is linear, the increment is determined by its gradient. In this case, the magnitude of the short-wave increment modulation is determined by the ratio of the turbulent velocity gradient to the average one. According to the estimates given in ref. 39, the assumption of the linearity of the velocity profile in the region of intense energy exchange is valid only for weak winds with friction velocities $u_* \sim 10$ cm/s and rather short waves with wave lengths $\lambda < 10$ cm. Troitskaya [40] calculated the increment modulation for this case in the framework of the quasi-laminar Miles model by taking viscous stresses into account. She showed that for weak winds and sufficiently long modulating waves, the oscillating component of the increment can be comparable with an average component.

At larger values of wind-friction velocities typical of moderate winds ($u_* < 20 - 50$ cm/s), the region of energy exchange between centimeter-long waves and the wind may be situated higher than the viscous sublayer and, hence, may be affected by turbulent fluctuations of the wind velocity. In this case, the short-wave increment is determined by the entire velocity profile $U(y)$, and the modulation depends on the relation between the oscillating and average components of the air-flow velocity rather than on the gradient ratio.

We suggest a simple model of this process. The flow above the water surface is represented as a two-layer fluid. The viscous sublayer is represented as a thin layer of nonviscous fluid at rest (molecular viscosity is neglected), while the logarithmic boundary layer, in which the velocity varies more smoothly and the turbulent viscosity is essential, is modeled as a layer of viscous fluid with a constant (turbulent) viscosity coefficient, uniformly moving with some velocity approximately equal to the flow velocity at the boundary of the viscous sublayer (of about $12u_*$ [41]). The short-wave increment modulation is calculated within the framework of this model.

The modulation of the short-wave spectra in the presence of long waves is estimated by using the model equation for the spectral density of short waves

suggested in ref. 38. When the elevation profile in a long wave is sinusoidal

$$\eta = a \cos [k(x - ct)],$$

and $F_0(K)$ is the short-wave spectrum in the absence of a long wave, the modulated short-wave spectrum has the form

$$F(K) = F_0(K) \{1 + mka \cos [k(x - ct) - \psi]\},$$

where m and ψ are the amplitude and the phase of the modulation coefficient. The results show that the value m sharply decreases with increase in wind velocity. This decrease is due to increase in the nonmodulated part of wind-increment of a short wave and, thus, to reduction of the time needed for effective interaction between a wave and a flow. A more consistent model of increment modulation in the presence of a turbulent wind will be developed.

3.6 Generation of internal waves by stratified flow around obstacles

The theory of IW generation in a stratified fluid is an intensively developed area of hydrodynamics (see, e.g., the review by Stepanyants et al. [42]). In the linear approximation, the IW excitation process is described by a set of equations:

$$\begin{aligned} \rho_0 \frac{\partial \vec{u}}{\partial t} + \nabla p &= \rho \vec{g}; \\ \frac{\partial \rho}{\partial t} + (\vec{u} \nabla) \rho_0 &= 0; \\ \operatorname{div} \vec{u} &= q(\vec{r}, t). \end{aligned} \tag{14}$$

Here $\rho_0(z)$ is the water density, ρ and p are the density and pressure perturbation, \vec{u} is the velocity field, $q(\vec{r}, t)$ is the distribution of the mass sources and sinks modeling the flow around an obstacle. For weak stratification ($F = \frac{UT_B}{d} > 1$, where U is the flow velocity, T_B is the Brunt-Väisälä

period, d is the characteristic size of the obstacle so that F is the corresponding Froude number), one can assume that the water flow close to the body is the same as in a nonstratified medium. This assumption enables choosing the same sources as those in a uniform fluid.

The solution of Eqs. (14) by means of integral transformations can be reduced to quadratures. Stationary-phase approximation is employed for a field in the far zone. Analytical formulae are obtained for only few types of stratification. In particular, in ref. 43 we considered the case of linearly stratified fluid and obtained expressions describing pressure perturbations in the medium as well as vertical displacements and horizontal velocities on the free surface. We showed that the surface perturbation is determined by the parameter $\alpha = NU/g$; in our case $\alpha \ll 1$, therefore IWs manifest themselves on the surface primarily by horizontal currents produced by them. The IW amplitude is inversely proportional to the Froude number (for $F > 1$). In a previous study [44], the vertical displacements of the free surface caused by IWs produced by the IW generator were measured experimentally under laboratory conditions. In another paper [45], the IW field and the related wave drag for two-layer stratification is described. As a source we have considered a model of a body oscillating in a uniform flow of the stratified fluid. The dependence of the wave drag on the motion velocity and on the body oscillation frequency were investigated, and the possibility of the instability of such an oscillating system due to wave radiation was demonstrated. The instability occurs for Froude numbers exceeding some critical value. A study of influence of viscosity on the radiation instability of oscillator motion in [46] showed that the degree of the viscosity influence depends on the Reynolds and Froude numbers and on the fluid-density ratio.

The problem with waves generated by a stratified shear flow around an obstacle is more complicated. In this case, the most interesting effects occur when the flow velocity at some horizon coincides with the body's velocity. At this level a critical layer appears, in which the wave-phase velocity coincides with the flow velocity, resulting in strong wave interaction with flow; thus, intense absorption, radiation, and strong refraction of IWs occur in their vicinity. Reznik and Troitskaya [47] modeled the stationary stratified flow with a constant shear U_{0z} and the buoyancy frequency N around a stationary two-dimensional obstacle with a characteristic width a under the condition of a dynamically stable flow. It was assumed that at some distance d from the surface there is a level where the flow velocity changes its direction. The

wave drag on the obstacle is given by

$$D = 4\pi\rho_0 \frac{h^2 U_0 N}{F^2} \int_0^\infty \Phi^2 \left(\frac{\kappa}{F} \right) f(\kappa, F) d\kappa \quad (15)$$

where $\Phi \left(\frac{\kappa}{F} \right)$ is the normalized spectrum of the surface elevation, $\kappa = kU_0/N$ is the normalized wave number, $F = U_0/Na$ is the Froude number, h is the obstacle height, f is the momentum flux carried by a harmonic wave with a wave number k and the unit amplitude. It has been demonstrated that at small and moderate Froude numbers, the wave drag is considerably higher than when the flow has a uniform velocity profile.

4 Planned Experiments and Preliminary Experimental Results

4.1 Internal-wave damping by small-scale turbulence

The IW damping by turbulence will be experimentally studied in the tank with a thermocline-type stratification

Some results have already been obtained in the small tank ¹. Figure 28 schematically shows the temperature profile typical of the SST and the designed setup. Turbulence was generated by a vibrating grid (4) and IWs, by the generator (wave maker) (7). The IWs were measured by two groups of sensors, one (6) close to the wave maker and another (2) after the turbulent region. The influence of reflected waves was reduced by a wave absorber (1). To sustain turbulence in a small region and to avoid rapid mixing of the entire bulk of water by the grid oscillations; we used plates (5) to separate the channel where the IWs were investigated. The turbulence was measured by means of the DISA anemometer (3).

Under the experimental conditions, the first IW mode (with the periods of 18 to 45 s, corresponding to the maximum efficiency of the wave maker) strongly prevailed (The minimal buoyancy period was about 17 s.) Preliminary measurements of the turbulence generated by the grid have been made.

¹The details of this experiment are described in the ref. 14 which has appeared after the Experimental Design Report was released.

The results showed that the turbulent energy decreases rather rapidly with depth, which is similar to the situation in a real ocean.

Figure 29 shows:

- the vertical distribution of the kinetic-energy density of turbulent pulsations for a grid oscillation-frequency of 5 Hz and a perforation scale of 2 cm;
- the dependence of the buoyancy frequency on depth;
- the first-mode vertical-velocity-component structures calculated for two wave numbers).

The results of measuring IW damping are presented in Fig. 30; they agree well with the theoretical model outlined above. Note that the theoretical curve and experimental points are not normalized by their maximal values, so that their closeness is informative.

We plan to perform a similar experiment in the large tank where the turbulence can be generated by a turbulent flow rather than by a grid (generators of such currents are included in the design of both tanks). This operational setup seems to be even more interesting from the viewpoint of modeling actual oceanic processes. However, the control and measurements of turbulence in the presence of a mean flow is a rather difficult problem to solve.

4.2 Surface-wave transformation by nonuniform flow around a moving sphere

To verify the theoretical model of SW transformation by a two-dimensional current, as described in section 2.2, we have planned an experiment in the LST.

In a laboratory experiment [48], one-dimensional, nonuniform current action on SWs was analyzed; the SWs propagated counter to a current that is nonuniform along the same direction. Variations in SW characteristics along the current were investigated, including observation of the blocking (group-synchronism) effect implying SW reflection from a point where its group velocity becomes smaller than the current speed. We plan to record a two-dimensional spatial distribution of the amplitude of the SW scattered

by a nonuniform flow corresponding to the dipole field (see section 2.2). The experimental parameters will be chosen to include the blocking effect in a two-dimensional configuration.

Our concept of the experiment is: a sphere will be moved under the water surface, and the SW transformation by nonuniform flow around the moving sphere in the adjacent reference frame will be recorded. The SW generator will be placed at the end of the tank from which the sphere is started. At the other end of the tank, SWs will be damped by a wave absorber. In the reference frame of the sphere, we obtain a physical situation adequate to that considered in section 2.2.

In the SST, we have previously performed a simpler version of such experiments, which have demonstrated the possibility of essential modulation of the SW amplitude above a moving sphere. An example of the experimental results is shown in Fig. 30. The water surface deviation shown in the figure was recorded by a contact string gauge placed 3 m from the Sw generator. The SW frequency f was 3.3 Hz, and its group velocity was slightly less than the velocity of the sphere motion ($\simeq 25$ cm/s). Stratification was not created in this experiment. In the limited vicinity of the moment t_0 when the sphere passes the gauge level, strong modulation of the surface wave amplitude occurred. Preliminary experiments demonstrated the resonant character of the effect: SW amplitude modulation is observed only at such frequencies for which the corresponding group velocity is close to the sphere velocity V .

According to the preliminary measurements, SWs with a frequency close to 2 Hz are most appropriate for the experiment in the LST. To satisfy the group-synchronism condition, the sphere will be moved at a 40 cm/s. It can be easily calculated that in the dimensionless units used in section 2.2, the tank width for this velocity will amount to 60. (Note that the measurements should be made in an even narrower region to avoid the influence of the tank walls.)

The water-surface deviation will be recorded by a set of wire wave gauges arranged transversely in the tank, and to register the moment when the sphere is passing the gauge line, a contact sensor will be used. Then we shall have a set of records similar to that exhibited in Fig. 31, but corresponding to different distances from the tank axis. This will enable us to determine the wave-amplitude variation for each case, with the assumption that the structure of anomalies does not change significantly when they pass the gauge line (this interval is about 100 dimensionless time units). The results of

these measurements will be used to reconstruct the spatial structure of SW amplitude variations.

Experiments involving SWs with the group velocities less than V , equal to V , and more than V are planned. The magnitude of perturbation can be controlled by varying both the size of the sphere and the depth of its motion. Temporal evolution of surface anomalies can be analyzed by setting sensors at various distances from the wave generator. Theoretical calculations of spatial distribution of the SW amplitude will be made, and the results will be compared with the experimental data at different wave frequencies.

4.3 Evolution of short trains of intense surface waves

Experimental investigations of intensive SW trains have actively been performed in the last few decades [19, 20]. As mentioned in section 2, the experimental results were treated within the framework of the nonlinear Schrödinger equation (NSE) for the wave envelope, without taking into account the dependence of the SW group velocity on wave intensity [20, 49]. A discrepancy between the experimental results and the theoretical model has been observed. In particular, study by Feir [19] deals with asymmetrical distortions of the train envelope that cannot be described within the framework of the NSE model. This is partly due to the fact that the SW generator operation conforms better to the nonstationary signaling problem than to the initial one analyzed in the theory [21].

We plan to investigate experimentally the propagation of short (a few wavelengths) wave packets of intense SWs having a symmetrical form at the initial point, in order to observe the self-steepening effect for such trains. This seems important for understanding the behavior of intense short-range gravity waves, which are important for remote sensing methods.

The experiments will be carried out in the LST ($20\text{m} \times 4\text{m} \times 2\text{m}$ m^3). Short SW trains will be generated at one end of the tank and will be absorbed at the other end. The expected absorption efficiency amounts to 85%. The water displacement amplitude near the SW generator region will be varied within the interval 1 to 3 cm. A SW pulse will be excited by five generator oscillations at a carrier frequency of 1.6 Hz ($\lambda = 58.5$ cm). Since for waves on deep water the phase velocity V_{ph} is twice as large as the group velocity V_g , the initial packet length will be $2.5\lambda \approx 145$ cm. The values of the water-surface deviation from equilibrium are to be measured at distances of 4, 6,

7, 8, 10, and 12 m.

Test experiments for the maximum initial amplitude of the water-surface displacement (3 cm) have already been carried out. Figure 32 shows the water-surface displacement at 4 and 6 m from the wave generator. At a distance of 4 m, the wave packet remains symmetric, whereas at 6 m, an intensity maximum occurs at the leading edge of the packet.

4.4 Thermocline excitation by the short trains of surface waves

Usually studies of SW propagation neglect the stratification of the subsurface layer. However, if the thermocline is situated close to the surface, it is displaced by the SW, which, consequently, may excite internal waves. The interaction between intense SW and the thermocline will be modeled in the LST with the thermocline location depth h being less than the SW length λ_s and much less than the IW length λ_i . The dependences of the water temperature T and of its gradient dT/dz as a function of depth z are given in Figs. 33 and 34, respectively. Figure 34 shows that the maximum value of dT/dz , corresponding to the thermocline center, is at a depth of 25 cm.

We plan to model the propagation of an intense SW packet generated at one end of the tank. The carrier frequency of the packet is expected to be 1.6 Hz (in this case $\lambda_s = 58.5$ cm), and the packet length, about 3 cm. The deviations of the fluid surface a_s and of the temperature ΔT from their equilibrium values at various depths in the vicinity of the thermocline center will be measured experimentally. Figure 35 shows preliminary experimental results obtained for the deviations of the fluid surface a_s [Fig. 35(a)] and of the isotherms from their equilibrium values at depths of 15 cm [Fig. 35(b)], 20 cm [Fig. 35(c)], and 25 cm [Fig. 35(d)] at 4 m from the wave maker. At a depth about 25 cm, corresponding to the thermocline maximum, the temperature variations are the strongest.

We also plan to investigate the opposing action of thermocline motion on the SW propagation.

4.5 Surface-wave damping caused by turbulence

Surface-wave damping due to turbulence will be modeled in the oval wind-wave tank by using the methods similar to those used to investigate IW

damping caused by small-scale turbulence in a thermost stratified tank. The method involves SW amplitude measurements at several points of the turbulent region. The wave maker can generate SWs with wavelength range 5 to 10 cm.

An oscillating grid 10 to 15 cm below the surface will create the turbulence. The grid area is 50 cm \times 20 cm; its perforation scale is 2 cm; its vibration frequency is variable from 3 to 15 Hz; and its oscillation amplitude can be variable from 0 to 2 cm.

A DISA flow meter will measure turbulent pulsations. According to the preliminary measurements, the turbulence generated by the grid at the frequency 6 Hz occupies a region about 1.5 m long, with grid oscillation amplitude of 1 cm.

Note that it is somewhat simpler to measure SW damping than the IW damping. Since the surface wavelengths are several times smaller than the IW wavelengths, while the turbulence region is limited in both cases, a less intensive (and, hence, more uniform) turbulence can be used. Besides, SW damping by a degenerating turbulence (i.e., when the grid is switched off) can be observed. On the other hand, future studies of the cases in which SW and turbulence have comparable scales are a possibility.

4.6 Nonlinear gravity-capillary waves and their modulation by internal waves

The generation of "parasitic" capillary-gravity ripples by short, steep gravity waves (with wavelengths from 4-5 cm to 25-30 cm) was observed earlier [28]. The first laboratory experiments demonstrating the mechanism of cascade modulation of ripples in the IW field are described in [29]. These studies are in their initial stage now, and the series of experiments planned includes

- investigation of the harmonic generation in short gravity SW including the dependence of harmonic amplitude on the fundamental wave amplitude;
- study of the cascade modulation of short SW harmonics and of the parasitic CGR for a wide range of SW and IW parameters.

These experiments will be carried out in the oval wind-wave tank. The first experimental run will be devoted to measuring slopes and curvatures of

SWs generated in the frequency band from 2.5 to 7 Hz for various SW amplitudes. The frequency spectra of SW slopes and the distribution functions of the SW curvature will be analyzed. We also plan to make preliminary measurements of spatial SW spectra with an optical spectrum analyser (OSA) in the wavelength range 3 mm to 5 cm. The next experimental run will study ripple modulation in the IW field. A two-layer stratification, internal wavelengths from 0.5 to 1 m and amplitudes from 0.5 cm to 2 cm will be used. We will concentrate on measuring SW curvature modulation. In the measurements with OSA are successful, we will then measure the modulation of intensities of the higher spatial harmonics of SWs under the influence of IWs and compare cascade modulation of the higher harmonics with the modulation of the fundamental SWs due to kinematic effects.

4.7 Nonlinear interactions of surface waves

The energy exchange between plane gravity SWs of different lengths will be studied experimentally. Four-wave interactions are known to be the most pronounced for gravity waves [7, 21] provided their frequencies ω_i and wave numbers \vec{k}_i satisfy the resonance conditions: $\sum_{i=1}^4 \vec{k}_i = 0$, $\sum_{i=1}^4 \omega_i = 0$ (the frequencies are given with their signs). Here, the rate of energy exchange is proportional here to $(ka)^2$, where a is the wave amplitude; so, it is rather weak for moderate slopes ($ka \leq 0.1$). This circumstance essentially dictates the experimental setup: in particular, a tank with a large surface area is needed. Nevertheless, different situations were considered (see, e.g., refs. 49-52), and some experiments on the interaction of two wave pairs propagating in mutually perpendicular directions have been performed [50, 51].

A novel idea of our planned experiments is to employ a tank area with reflecting walls (a resonator). Its eigenmodes are longitudinal, transverse, and diagonal standing waves (this specifies propagation direction with respect to the wall orientation); each is equivalent to a pair of counterpropagating traveling waves. The simplest case to be studied is that in which the frequencies ω_i of all four traveling waves are the same, and the propagation directions are pairwise opposite: $-\vec{k}_1 = \vec{k}_2$, $-\vec{k}_3 = \vec{k}_4$. In the experiment, the wave frequency ω and the resonator length L should be chosen in such a way that two standing modes are simultaneously resonant, one being the longitudinal and

the other either transverse (i.e. $\vec{k}_1 \cdot \vec{k}_2 = 0$), or diagonal ($\vec{k}_3 \cdot \vec{k}_4 \neq 0$). If, for example, the longitudinal mode is generated by the wave maker, instability will cause the transverse mode (or the diagonal one) to also be excited. The latter's amplitude growth can be observed by using a wave-recording gauge until steady-state oscillation regime is established, if possible.

The laboratory setup designed for the SW interaction study consists of a resonator, a wave maker and wave-recording gauges. The resonator is a channel with a width $d = 0.2$ m, a depth $H = 0.5$ m, and a length $L = 3.2$ m. At one end it is limited with a vertical transverse wall providing practically complete reflection, and at the other end, with a partition that cuts off the channel up to the depths of 0.05 to 0.07 m. It reflects at least 80% of the incident wave energy and provides a weak coupling between the resonator and the wave maker. The partition, together with the wave maker, can be placed at any distance up to 3 m from the transverse wall of the channel. The wave maker is an electromagnetically driven, rectangular plastic-foam rod ($0.07 \text{ m} \times 0.0702 \text{ m} \times 0.02 \text{ m}$) partially submerged in the water. Wire gauges of different types will be used for recording wave amplitude.

Using this setup, we will carry out the following experiments:

1. Measure the dependence of nonlinear additions to the phase velocity of two corunning or counterrunning waves on their amplitudes.
2. Measure the dependence of the amplification factor of a wave pair on the amplitude of an another pair for various angles between the wave vectors of interacting pairs.

4.8 Determination of surface wave-parameters with optical and radar techniques

Laboratory investigation of the space - time structure of small - scale SWs is important for better understanding of many oceanic and atmospheric processes. Such investigations are often difficult to carry out with point sensors, such as wire gauges. Optical methods based on the spectral analysis of SW images and radar methods are most suitable for measurements of the space - time characteristics of SWs. Passive optical methods are easily adaptable for various wavelengths, from millimeters to tens of meters, and they are suitable for both field and laboratory conditions.

In experiments devoted to the investigation of two-dimensional space

spectra of wave slopes [53-55], the spread - light source was placed at the bottom of the water tank. The SW images were recorded by a nadir - looking CCD camera with a short exposure time. However, space-time characteristics of short SWs were not studied in these works, apparently because measurement of high-frequency spectra of ripples is limited by the repetition rate of a CCD camera.

We have developed incoherent OSAs for space - time spectral analysis in real time of SW images at wavelengths from a few meters to a few millimeters [1,2]. These optical devices can be divided into groups to record the following in real-time:

- 2D-space spectra of the SW slopes. For example, the spectra at wavelengths from about 7 cm to 1.5 m were recorded from a ship or a sea platform [56];
- space-time spectra of sea waves as a function of frequency for several wave numbers;
- space-time optical images of SWs with wavelengths of 2 m and more, similar to radar images.

These images enable determination of the kinematic and spectral characteristics of long sea waves [57]. The optical devices have a high sensitivity and a large dynamical range, and, they can be used under either laboratory or field conditions (on board a ship or a sea platform). The PC software was developed for recording data supplied by these devices on a hard disk and for imaging these data on a TV monitor in real time.

Some theoretical problems associated with optical imaging of wind waves under field conditions have been considered. The two-scale model of short-long wind waves was employed in a way similar to a model of electromagnetic wave scattering [58]. The dynamic characteristics of the short-wave image were shown to depend not only on the orbital velocity of the long wave but also on its height. The main results are described below.

The mean frequency of space - time spectra of SWs depends on the phase velocity of short waves, the velocity of a surface current and surface wave drift. The dispersion of frequency fluctuations σ_f^2 is determined by the ex-

pression:

$$\sigma_f^2 = \frac{1}{\lambda^2} \left[\left\langle \left(\vec{v}_0 \cdot \vec{j} \right)^2 \right\rangle + \frac{1}{\tan^2 \beta} \left\langle \left(\frac{\partial a}{\partial t} \right)^2 \right\rangle \right], \quad (16)$$

where λ is the short-wave length, a is the long-wave elevation, \vec{v}_0 is the horizontal orbital velocity of a long wave, β is the observation angle, and \vec{j} is the unit horizontal vector in the observation direction. The contribution of the orbital velocity or of the long-wave elevation to the space-time spectra of short waves depends on the observation angle. For a simple model of a long, harmonic surface wave, the expression for σ_j^2 will be:

$$\sigma_j^2 = \frac{\sigma_h^2 \omega_0^2}{2\lambda^2} \left[\left(\vec{k}_0 \cdot \vec{j} / k_0 \right)^2 + \frac{1}{\tan^2 \beta} \right],$$

where σ_h^2 is the dispersion of long - wave elevations, and ω_0^2 and \vec{k}_0 are the frequency and the wave vector of a long wave.

This expression has been experimentally verified, and an optical method is proposed for measuring long-wave parameters from the space - time spectra of a short - wave image.

For the large tank, we plan to create an optical system for recording space - time SW parameters at wavelengths from several decimeters to millimeters that includes optical spectrum analyzers and the CCD TV camera. A hermetic gradient light source (1.5 m \times 1.5 m), similar to that described in refs 53 and 54, will be installed somewhere on the tank bottom, a nadir - aimed optical sensor will be placed above the water surface, and a light source will be mounted at a height of about 2 m. Besides calculating the relation between the brightness of the water - surface image and wave slopes and measuring the accuracy of space - time characteristics of SWs, a probe harmonic gravity wave will be used to test the optical system. The gravity waves will be generated by a mechanical wave maker; their profile will be verified by wire gauges. We plan to develop a theory of optical remote sensing of space - time spectra of ripples generated on the long wave profile based on the two-scale model of water waves. For example, a method can be suggested for recording spectral - density variations of short waves by using the space-time spectra of a surface image.

Note that Keller and co-workers [55] used both an optical analyser and the X-band scatterometer to measure spatial spectra of ripples to verify models

of electromagnetic scattering by rough surfaces. We plan to carry out a comparative investigation of the space - time spectrum of centimeter-range waves by using an OSA and the specially designed X-band scatterometer.

5 Acknowledgments

The cooperation with the NOAA Environmental Technology Laboratory and the support from the joint NOAA/DOD Advanced Sensor Application Program are greatly appreciated.

6 References

1. E. M. Zuykova, A. G. Luchinin, and V. I. Titov. The determination of space - time characteristics of surface waves using an optical image of sea surface. *Izv. Akad. Nauk SSSR, Fiz. Atmosfery i Okeana*, **22**, v. 10, 833 - 837 (1985).
2. V. V. Bakhanov, D. M. Bravo-Zhivotovsky, E. I. Dorfman. A computer ship complex of remote sensing for investigation of ocean subsurface processes. *Black Sea '92 Proceedings Digest*, Varna, Bulgaria, 24 - 26 (1992).
3. S. A. Ermakov and S. G. Salashin. Modulation of gravity-capillary waves in the internal wave field. *Izv. Akad. Nauk SSSR, Fiz. Atmosfery i Okeana*, v. 20, no. 5, 394-404 (1984).
4. E. M. Zuykova, A. G. Luchinin, and V. I. Titov. Optical study of the variability of the surface wave spectrum in the internal wave field. In *Effect of intense internal waves on the sea surface*, Institute of Applied Physics, Gorky, 137 - 146 (1982).
5. Yu. Z. Miropolsky. *Dynamics of Internal Gravity Waves in the Ocean*. Gidrometehizdat, Leningrad, 1981.
6. A. S. Monin and R. V. Ozmidov. *Turbulence in the Ocean*. Dordrecht-Kluwer, Boston, 1985.

7. O. M. Phillips. *The Dynamics of the Upper Ocean*, 2nd ed., Cambridge University Press, New York, 1977.
8. G. I. Barenblatt. *Similarity, Self-similarity, Intermediate Asymptotics*. Gidrometeoizdat, Leningrad, 1978.
9. P. H. LeBlond. On the damping of internal gravity waves in a continuously stratified ocean. *J. Fluid Mech.*, v. 25, 121 - 142 (1966).
10. L. A. Ostrovsky and I. A. Soustova. Upper mixed layer of the ocean as an energy sink of internal waves. *Okeanologiya*, no.6, 973-981 (1979).
11. A. V. Ivanov, L. A. Ostrovsky, I. A. Soustova, and L. Sh. Tsimring. Interaction of internal waves and turbulence in the ocean. *Dyn. Atmos. Oceans*, v. 7, no. 4, 221 - 232 (1983).
12. L. A. Ostrovsky and D. V. Zaborskikh. Damping of internal gravity waves by small-scale turbulence. *J. Phys. Oceanogr.*, v. 26, no. 3, 388 - 397 (1996).
13. L. A. Ostrovsky, V. I. Kazakov, P. A. Matusov, and D. V. Zaborskikh. *Ibid.*, 398 - 405.
14. D. J. Olbers. Models of the oceanic internal wave field. *Rev. Geophys., Space Phys.*, v. 21, 1567 - 1606 (1983).
15. W. D. McKee. Waves on a shearing current: a uniformly valid asymptotic solution. *Proc. Cambr. Philos. Soc.*, v. 75, part 2, 295 - 301 (1974).
16. M. S. Longuet-Higgins and R. W. Stewart. Changes in the form of short gravity waves on long waves and tidal currents. *J. Fluid Mech.*, v. 8, no. 4, 565 - 585 (1960).
17. M. S. Longuet-Higgins and R. W. Stewart. The changes in amplitude of short gravity waves on steady non-uniform currents *J. Fluid*

Mech., v. 10, no. 4, 529 - 549 (1961).

18. A. Ya. Basovich and V. I. Talanov. On the transformation of short surface waves on non-uniform currents. *Izv. Akad. Nauk SSSR, Fiz. Atmosfery i Okeana*, v. 13, no. 7, 766 - 773 (1977).

19. J. E. Feir. Discussion: Some results from wave - pulse experiment. *Proc. R. Soc. London*, v. A299, 54 - 60 (1967).

20. T. B. Benjamin and J. E. Feir. The disintegration of wave trains on deep water. Part 1, Theory. *J. Fluid Mech.*, v. 27, 417 - 430 (1967).

21. G. Yuen and B. Lake. *Nonlinear dynamics of gravity waves in deep water*. Mir, Moscow, 1987, 179 p. (transl. from English).

22. K. B. Dysthe. Note on a modification to the nonlinear Shrodinger equation for application to deep water. *Proc. R. Soc. Lond., A*, v. 369, 105 - 114 (1979).

23. L. A. Ostrovsky. 1963. Electromagnetic waves in nonlinear media with dispersion. *Zh. Tekh. Fiz.*, v. 33, no. 8, 905 - 908 (1963) [English transl.: *Sov. Phys. Techn. Phys.*, v. 8, no. 8, 679 - 681 (1964)].

24. S. A. Akhmanov, V. A. Vysloukh, and A. S. Chirkin. Wave packets self-action in a nonlinear medium and the femtosecond laser pulses generation, *Usp. Fiz. Nauk*, v. 149, no. 3, 449 - 459 (1986) [English transl.: *Sov. Phys. Advances*, v. 149, 350 - 383].

25. L. A. Ostrovsky. Propagation of wave packets and space-time self-focusing in a nonlinear medium. *Zh. Eksp. Teor. Fiz.*, v. 51, 1189 - 1194 (1966) [English transl.: *Sov. Phys. JETP*, v. 24, no. 4, 797 - 800 (1967)].

26. L. N. Sretensky. *Theory of Wave Motions of Fluid*, Nauka, Moscow, 1975.

27. M. S. Longuet-Higgins. The generation of capillary waves by steep gravity waves. *J. Fluid Mech.*, v. 16, 138 - 159 (1963).

28. S. A. Ermakov, K. D. Ruvinsky, S. G. Salashin, and G. I. Freidman. Experimental investigation of capillary-gravity ripple generation by strongly nonlinear waves on the deep fluid surface. *Izv. Atmos. Ocean. Phys.*, v. 22, 835 - 842 (1986).
29. S. A. Ermakov, K. D. Ruvinsky, and S. G. Salashin. Local relationship between ripples on gravity-capillary wave crests and their curvature, *Izv. Atmos. Ocean. Phys.*, v. 24, 561 - 563 (1988).
30. K. D. Ruvinsky, F. I. Feldstein, and G. I. Freidman. Numerical simulation of the quasi-stationary stage of ripple excitation by steep gravity-capillary waves, *J. Fluid Mech.*, v. 230, 339 - 353 (1991).
31. A. Ya. Basovich, V. V. Bakhanov, and D. M. Bravo-Zhivotovskiy. On the correlation of spectral density variations of centimeter and decimeter surface waves in the internal wave field. *Dokl. Akad. Nauk SSSR*, v. 298, 967 - 971 (1988).
32. A. Ya. Basovich, V. V. Bakhanov, and V. I. Talanov. Transformation of wind waves by short trains of internal waves. *Izv. Akad. Nauk SSSR, Fiz. Atmosfery i Okeana*, v. 23, no. 7, 694 - 706 (1987).
33. S. A. Ermakov S. G. Salashin. On the effect of strong modulation of capillary-gravity ripple by internal waves. *Dokl. Akad. Nauk SSSR*, v. 337, no. 1, 108 - 111 (1994).
34. J. R. Apel. An improved model of the ocean surface wave vector spectrum and its effects on radar backscatter. *J. Geophys. Res.*, v. 99, no. 16, 269 - 291 (1994).
35. J. A. Smith. Modulation of short wind waves by long waves. In *Surface Waves and Fluxes*, v. 1, 247 - 284, Academic Publishers, Kluwer, The Netherlands, 1990.
36. O. M. Phillips, The dispersion of short wavelets in the presence of a dominant long wave. *J. Fluid Mech.*, v. 107, 465 - 485 (1981).

37. J.-H. Shyu and O. M. Phillips. The blockage of gravity and capillary waves by longer waves and currents. *J. Fluid Mech.*, v. 217, 115 - 141 (1990).
38. G. R. Valenzuela and J. W. Wright, Modulation of short gravity-capillary waves by longer-scale periodic flows: A higher-order theory. *Radio Sci.*, v. 14, 1099 - 1110 (1979).
39. T. B. Benjamin. Shearing flow over a wave boundary. *J. Fluid Mech.*, v. 6, 513 - 532 (1959).
40. Yu. I. Troitskaya, Yu. I. Modulation of the growth rate of short surface capillary-gravity wind waves by a long wave. *J. Fluid Mech.*, v. 273, 169 - 187 (1994).
41. A. S. Monin and A. M. Yaglom. *Statistical Hydromechanics, Part 1*. Gidrometeoizdat, St. Petersburg, 1992, 696 pp.
42. Yu. A. Stepanyants, I. V. Sturova, and E. V. Theodorovich. Linear theory of surface and internal wave generation. *Itogi Nauki i Tekh., VINITI, Mekh. Zhidkosti i Gaza*, v. 21, 93 - 179 (1987).
43. V. P. Dokuchaev and I. S. Dolina. Generation of internal waves by sources in an exponentially stratified fluid. *Izv. Akad. Nauk SSSR, Fiz. Atmosfery i Okeana*, v. 13, no. 6, 655- 663 (1977).
44. I. S. Dolina, S. A. Ermakov, V. V. Papko, and E. N. Pelinovsky. Experimental investigation of free surface oscillations produced by internal waves. *Ibid.*, v. 14, no. 11, 1216 - 1218 (1978).
45. A. V. Gaponov-Grekhov, I. S. Dolina, and L. A. Ostrovsky. Anomalous Doppler effect and radiation instability of oscillators in hydrodynamics. *Dokl. Akad. Nauk SSSR*, v. 268, no. 4, 827 - 831 (1983).
46. I. S. Dolina. Amplification of body oscillations in a stratified fluid. *Izv. Akad. Nauk SSSR, Mekh. Zhidk. i Gaza*, v. 4, 87 - 93 (1984).
47. S. N. Reznik and Yu. I. Troitskaya. Wave drag of localized obstacle

of the bottom to a stratified shear flow having a critical layer. *Izv. Akad. Nauk SSSR, Fizika Atmosfery i Okeana* (in press).

48. S. I. Badulin, K. V. Pokazeev, and A. D. Rozenberg. Laboratory investigation of regular gravity-capillary wave transformation on nonuniform currents. *Izvestiya Akad. Nauk SSSR, Fizika Atmosfery i Okeana*, v. 19, no. 10, 1035 - 1041 (1983).

49. M. S. Longuet-Higgins. Resonant interactions between two trains of gravity waves, *J. Fluid Mech.*, v. 12, pt. 3, 321 - 332 (1962).

50. L. F. McGolrick, O. M. Phillips, N. Huang, and T. Hodson, 1966. Measurements on resonant wave interactions. *Ibid.*, v. 25, 437 - 456 (1966).

51. M. S. Longuet-Higgins and N. D. Smith. An experiment on third order resonant wave interactions. *Ibid.*, v. 25, 417 - 435 (1966).

52. D. E. Hasselmann. The high wavenumber instabilities of a Stokes wave. *Ibid.*, v. 14, 491 - 499 (1979).

53. W. C. Keller and B. L. Gotwols. Two-dimensional optical measurements of wave slope. *Appl. Opt.*, v. 22, no. 2, 3476 (1983).

54. B. Jahne K. S. Riemer. Two-dimensional wave number spectra of small-scale water surface waves. *J. Geophys. Res.*, v. 95, no. C7, 11531 - 11546 (1990).

55. M. R. Keller, B. L. Gotwols, W. J. Plant, and W. C. Keller. Comparison of microwave backscatter with optically-derived cross-sections from wind-generated waves in a wave tank, *IGARSS'94*, IEEE Publications, Piscataway, NJ, 2424-2426 (1994).

56. V. V. Bakhanov (first author). Nonlocal effects of internal waves on the ocean surface. *Ibid.*, p. 760.

57. V. I. Titov (first author). Investigation of variations of long surface wave parameters by optical technique during JUSREX 1992. *Ibid.*, p.763.

58. E. M. Zuykova and V. I. Titov. Remote sensing of space - time characteristics of gravity waves using an optical method. Preprint no. 336, Institute of Applied Physics,, Nizhny Novgorod, Russia, 1995.



Fig. 1. Large thermostratified tank (overall view)

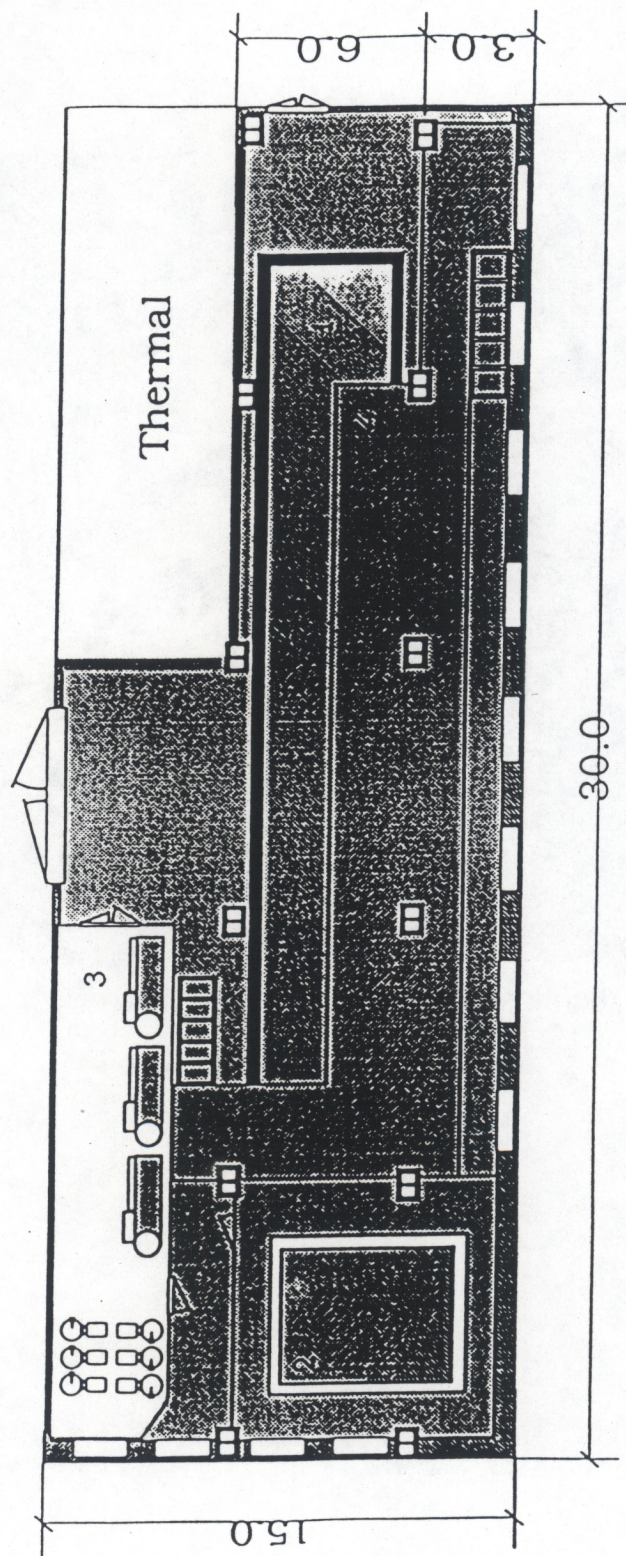


Fig. 2. Sketch of the hydrophysical laboratory: 1 - large thermostated tank (length 20 m, width 4 m, depth 2 m).
 2 - hydroacoustic anechoic tank (length 5.3 m, width 4 m, depth 2 m)
 3 - space for technological equipment (two refrigerators with total capacity of 47 000 kcal/h; one with capacity of 33 000 kcal/h; 6 pumps; automatic control system). Dimensions are in meters.

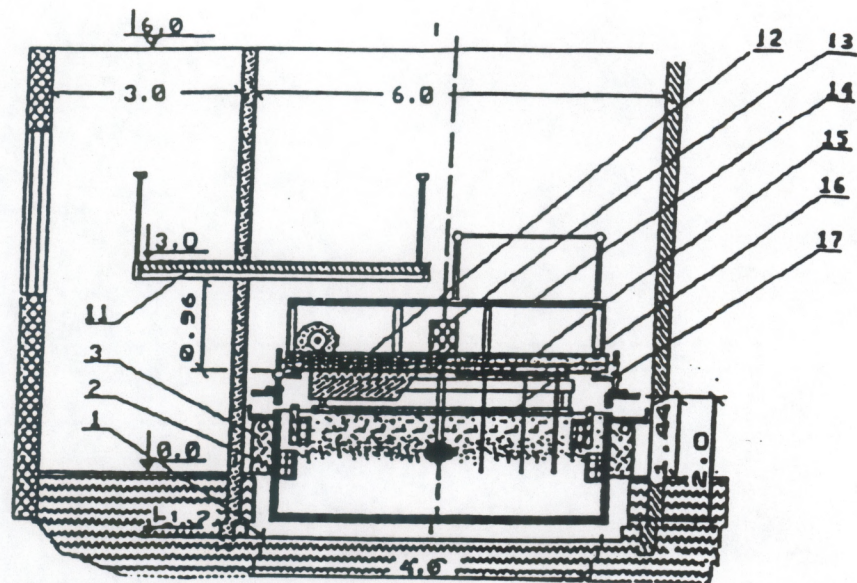


Fig. 3. Large stratified tank (section): 1 - concrete foundation with drainage; 2 - hydrochannel; 3 - thermal insulator; 11 - operating platform; 12 - towing trolley; 13 - two-component dynamometer; 14 - operating platform on the trolley; 15 - coordinate system; 16 - SW generator; 17 - rail.

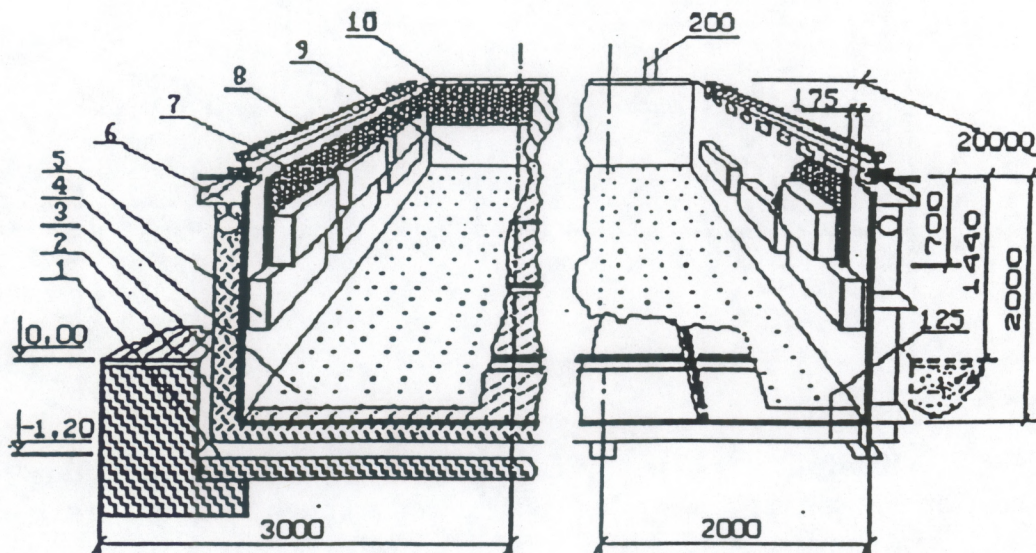


Fig. 4. Large stratified tank: 1 - foundation (concrete bowl with independent return line); 2 - hydrochannel; 3 - Thermal insulator; 4 - second bottom; 5 - heat exchangers; 6 - overflow ports; 7 - steel, thermal-insulated baffles with heat exchangers; 8 - rails for towing trolley; 9 - second vertical walls; 10 - thermal insulator (polyurethane).

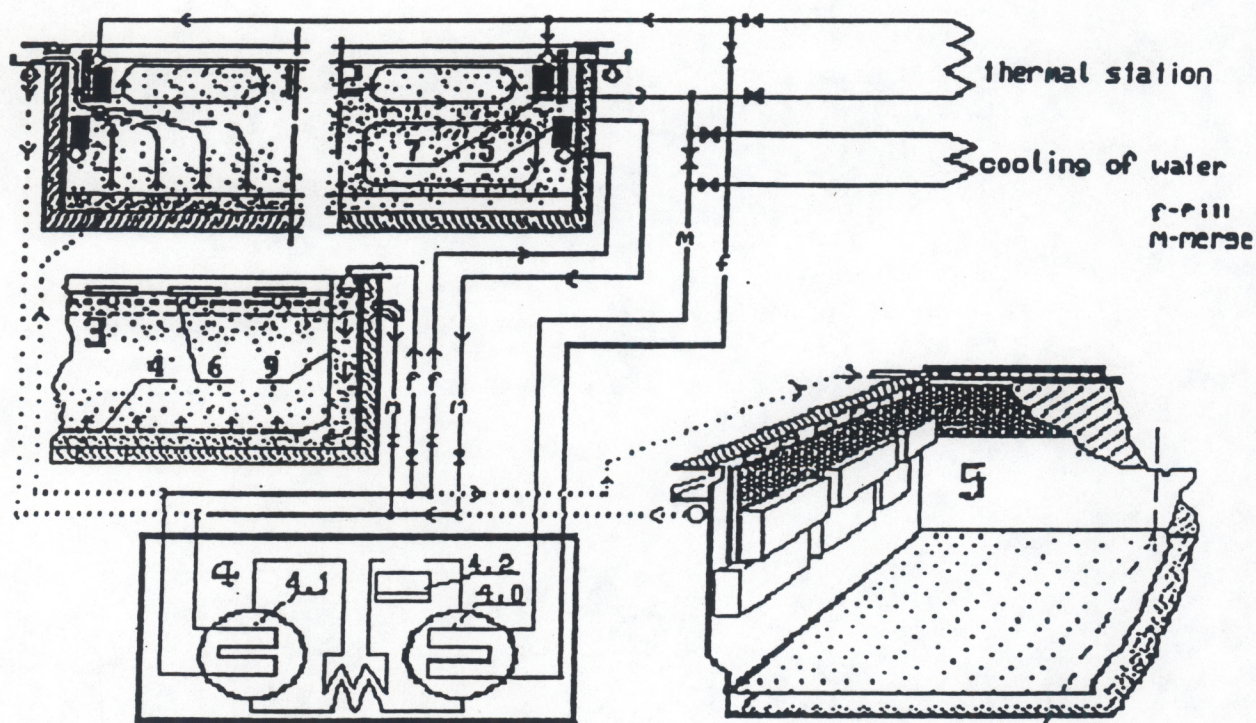


Fig. 5. Temperature stratification. 1, 2 - tank cross sections (lines with arrows show the convective currents during (1) generation and (2) maintenance of thermal stratification); 3 - longitudinal section (currents of water cooled by refrigerator is shown from the bottom and face ducts); 4 - refrigerator (4.1 - evaporation and cold - circuit pipelines; 4.2 - compressor; 4.3 - condenser and warm - circuit pipelines); 5 - sketch of the face of the hydrochannel with heat exchangers, heat - insulated baffles, overflow ports, and perforated second bottom (cf. Fig. 1.4).

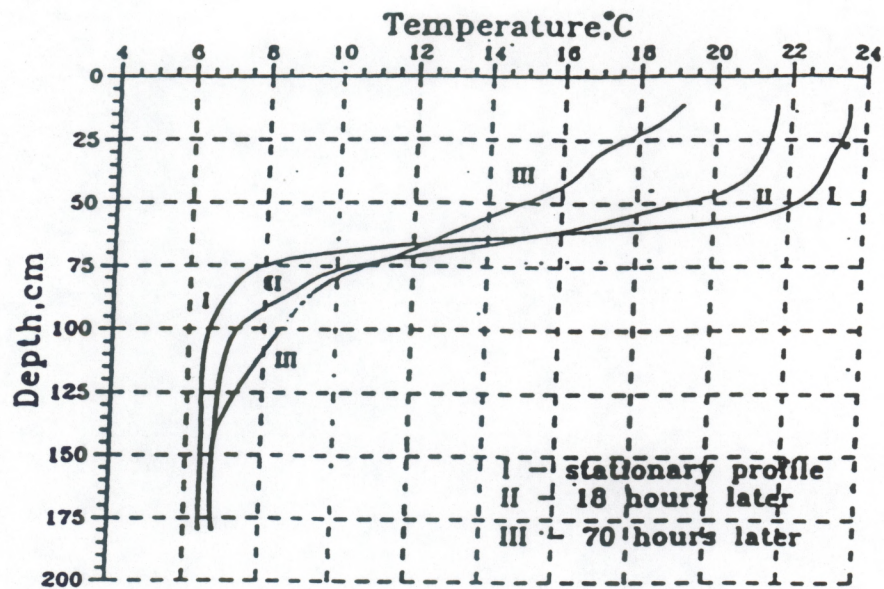


Fig. 6. Temperature profiles of relaxation for 18 h and 70 h after maintainig of stratification is ceased.

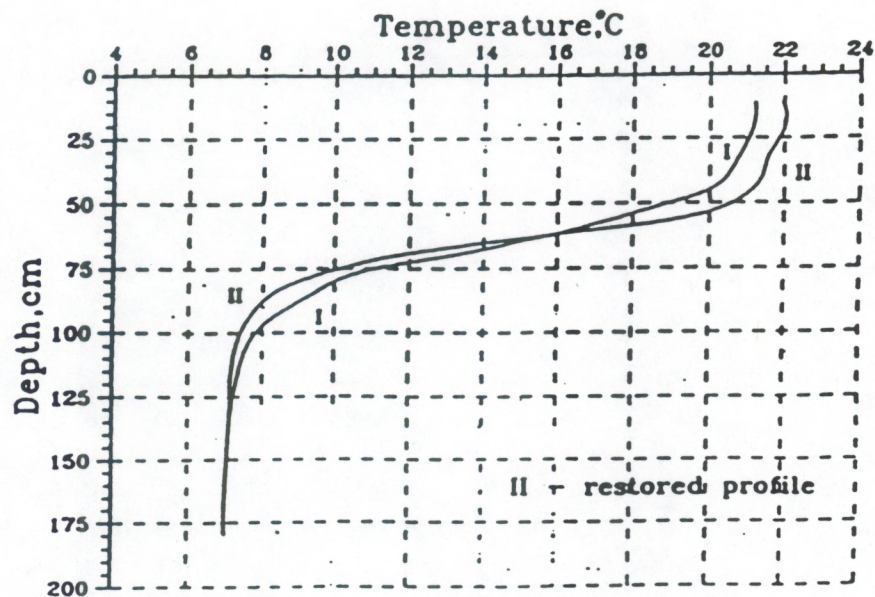


Fig. 7. Restoration of the temperature profile after 3 h of operation of the two large refrigerators.

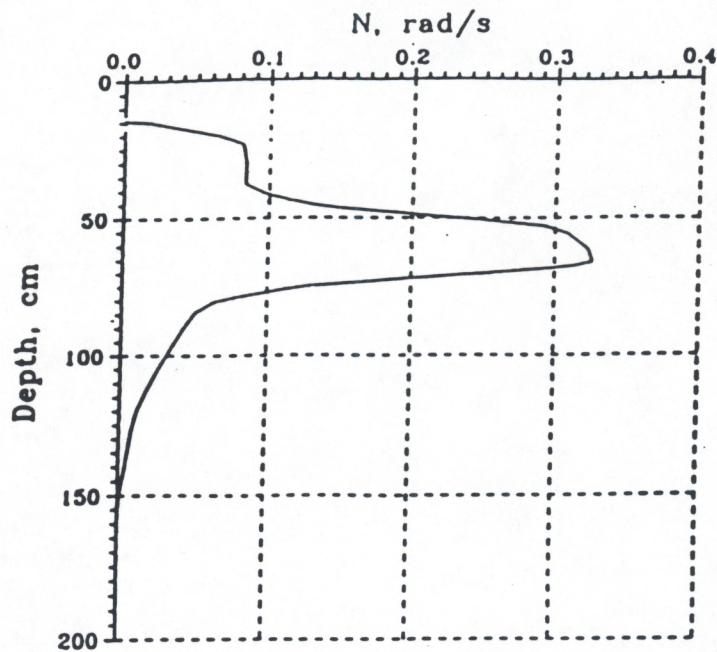


Fig. 8. Brunt - Vaisala frequency (N) profile: deep thermocline.

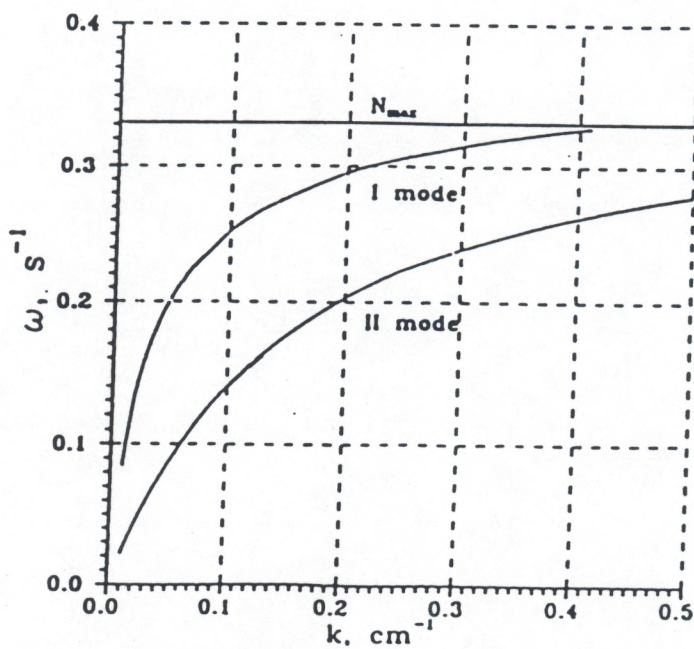


Fig. 9. Dispersion curves, $\omega(k)$, for the first two internal - wave modes.

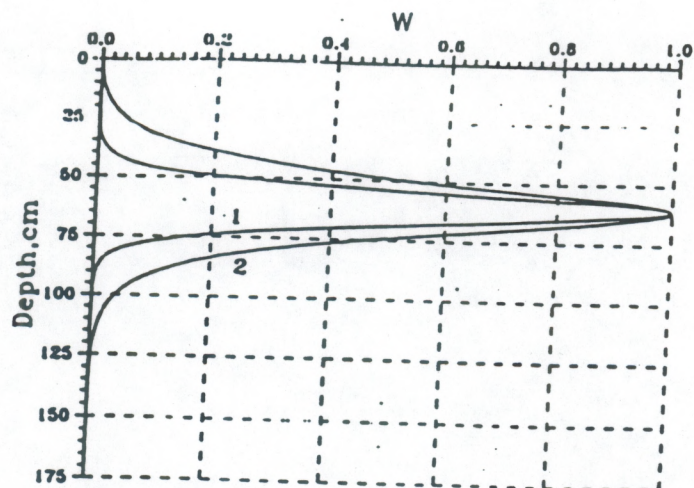


Fig. 10. Profile of vertical velocity of the 1st IW mode in deep thermocline: 1 - $\lambda = 0.5$ m ($k = 0.12$ cm $^{-1}$); 2 - $\lambda = 1.25$ m ($k = 0.05$ cm $^{-1}$).

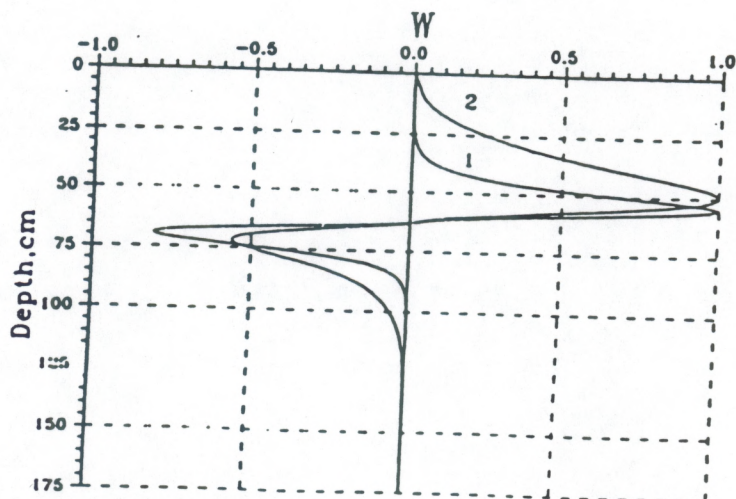
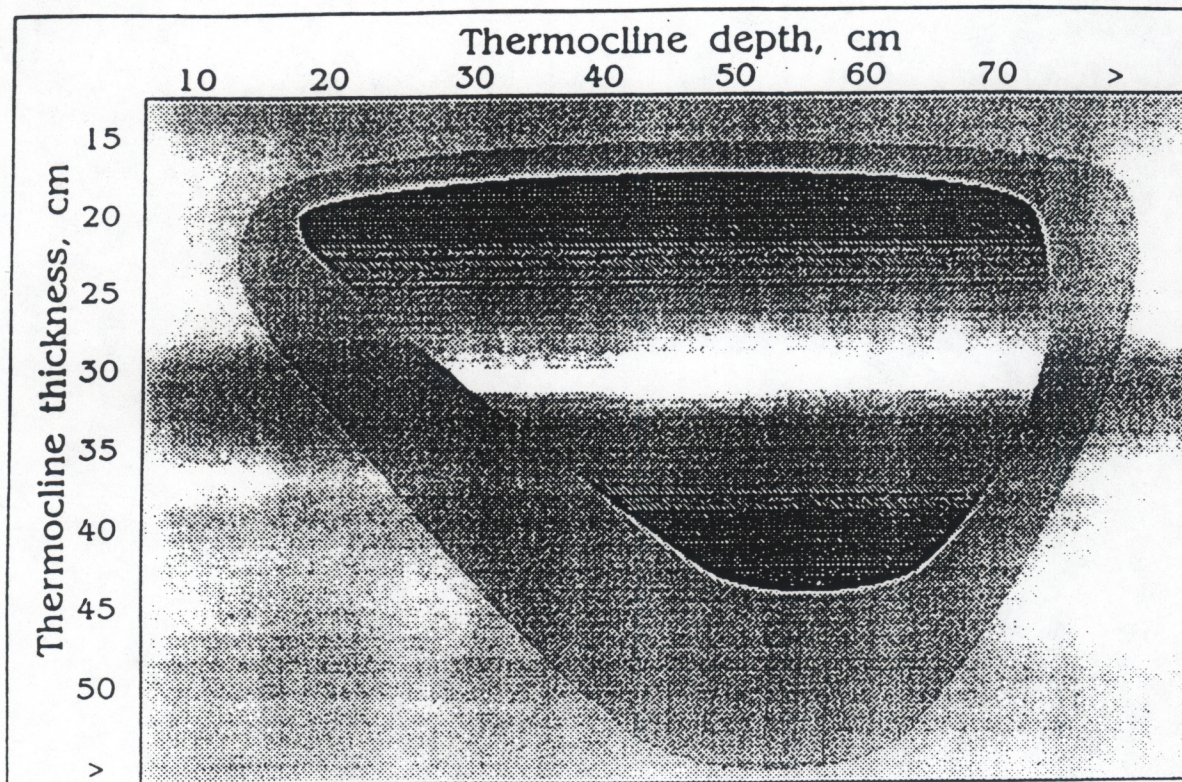


Fig. 11. Profile of vertical velocity of the 2nd IW mode in deep thermocline: 1 - $\lambda = 0.5$ m ($k = 0.12$ cm $^{-1}$); 2 - $\lambda = 1.25$ m ($k = 0.05$ cm $^{-1}$).






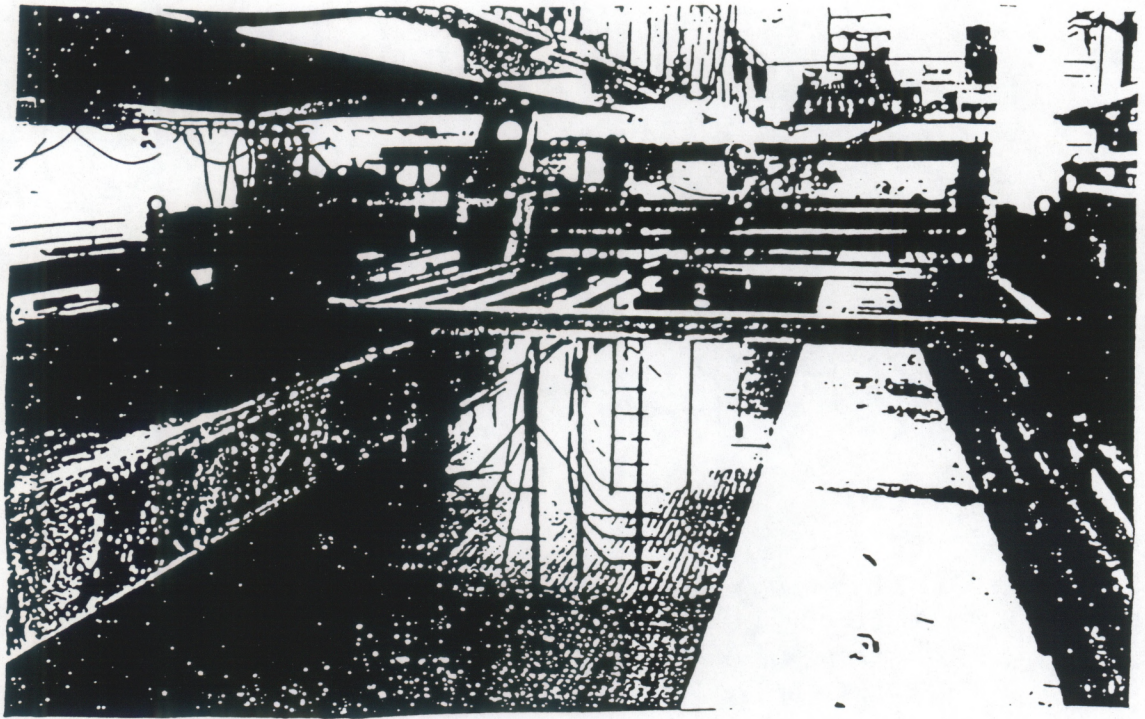
-  Temperature profiles that can be reached and maintained for a long time.
-  Nonstationary temperature profiles that can be maintained during 3 to 6 h.
-  Unattainable or uninvestigated temperature profiles.

Fig. 12. Types of stratification in the large tank.



(A)

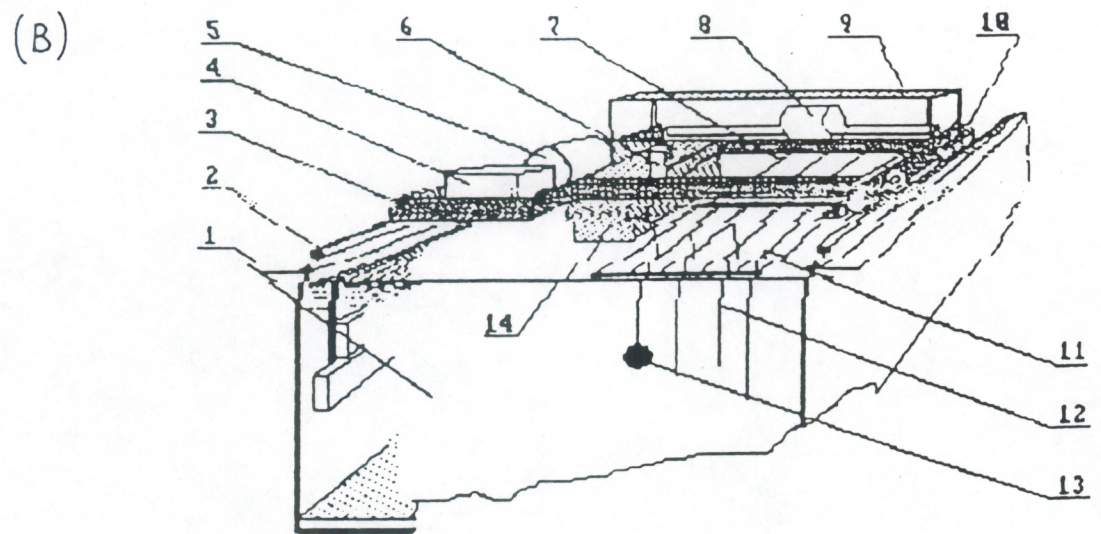
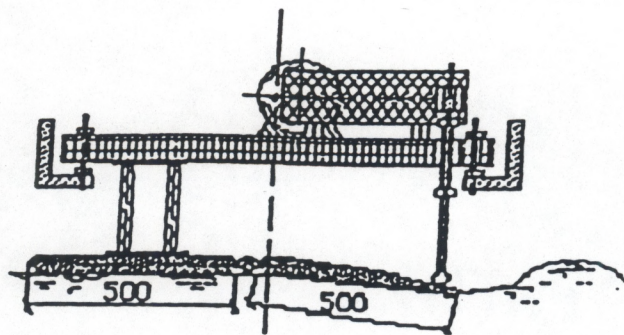


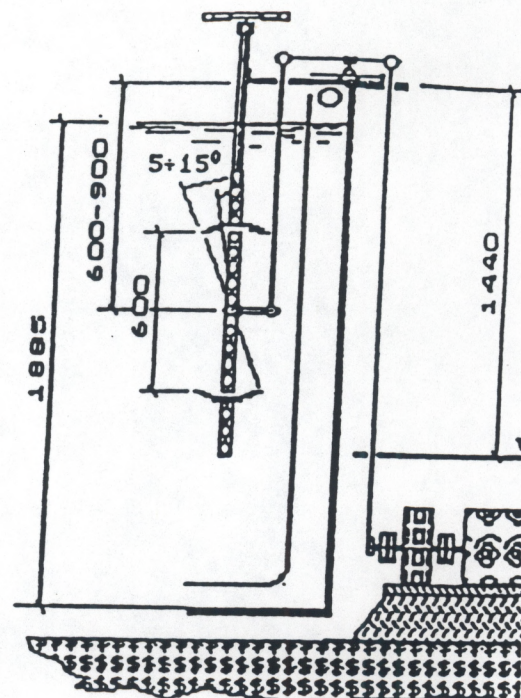
Fig. 13. Towing trolley:

A) General view; B) Design:

1 - basin; 2 - railtrack; 3 - carrier; 4 - reduction gear; 5 - motor; 6 - X and Y dynamometers; 7 - inside coordinate system; 8 - SW generator; 9 - platform for operators; 10 - wheel; 11 - outside coordinate system; 12 - bar for sensing elements; 13 - test model.



(a)



(b)

Fig. 14. Wave generators for (a) surface waves ($f = 0.1 - 0.4$ Hz) and (b) internal waves ($f = 0.008 - 0.03$ Hz). Dimensions are in millimeters.

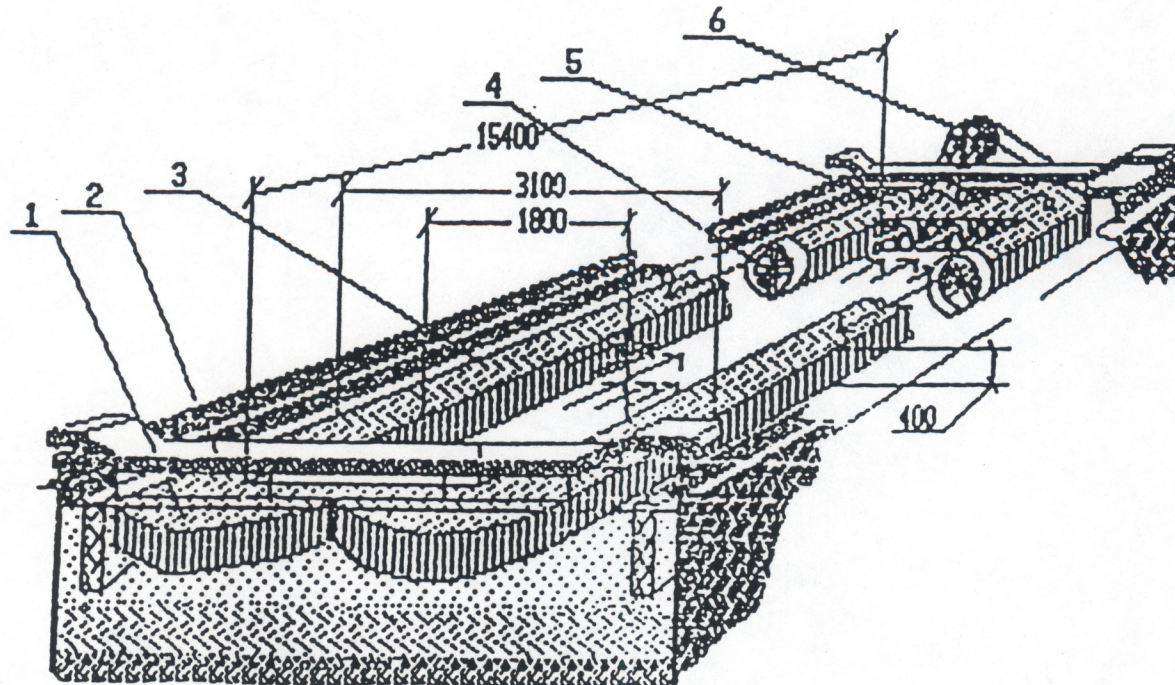


Fig. 15. Flow inductor:
1 - nozzle block; 2 - platform; 3 - water line; 4, 5 - water intake set;
6 - motor.

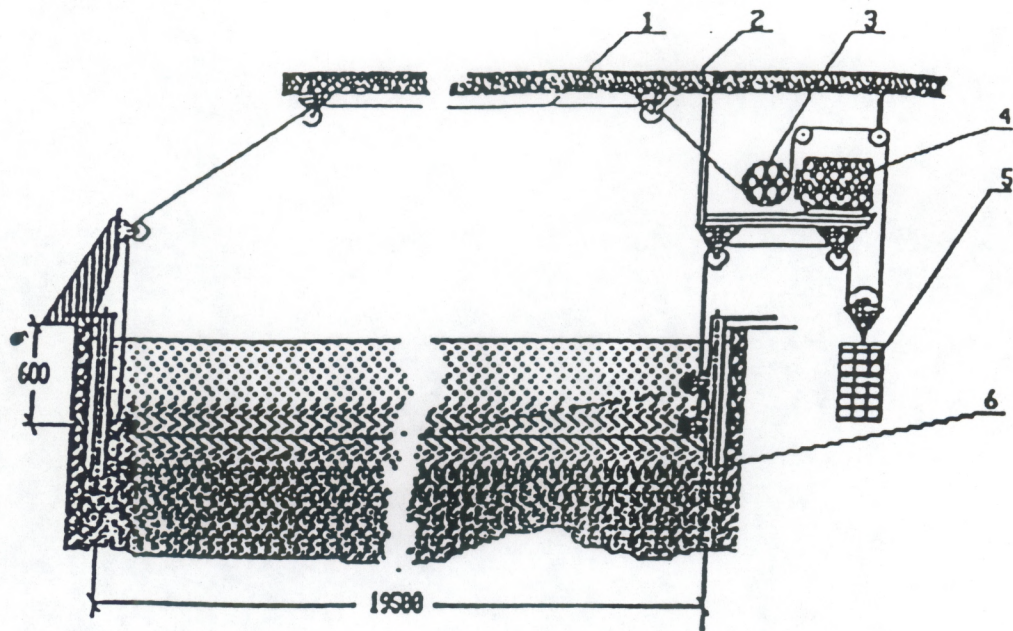


Fig. 16. The rope towing system:
1 - cable; 2, 3 - guide rollers; 4 - motor.
Sizes are in mm.

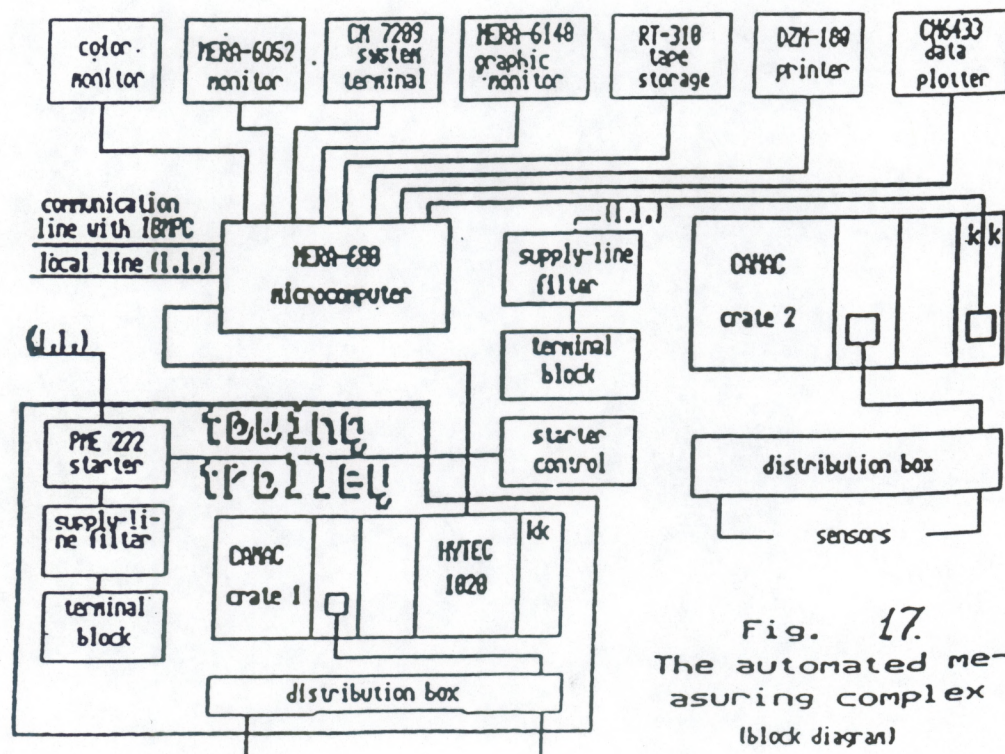


Fig. 17.
The automated measuring complex
(block diagram)

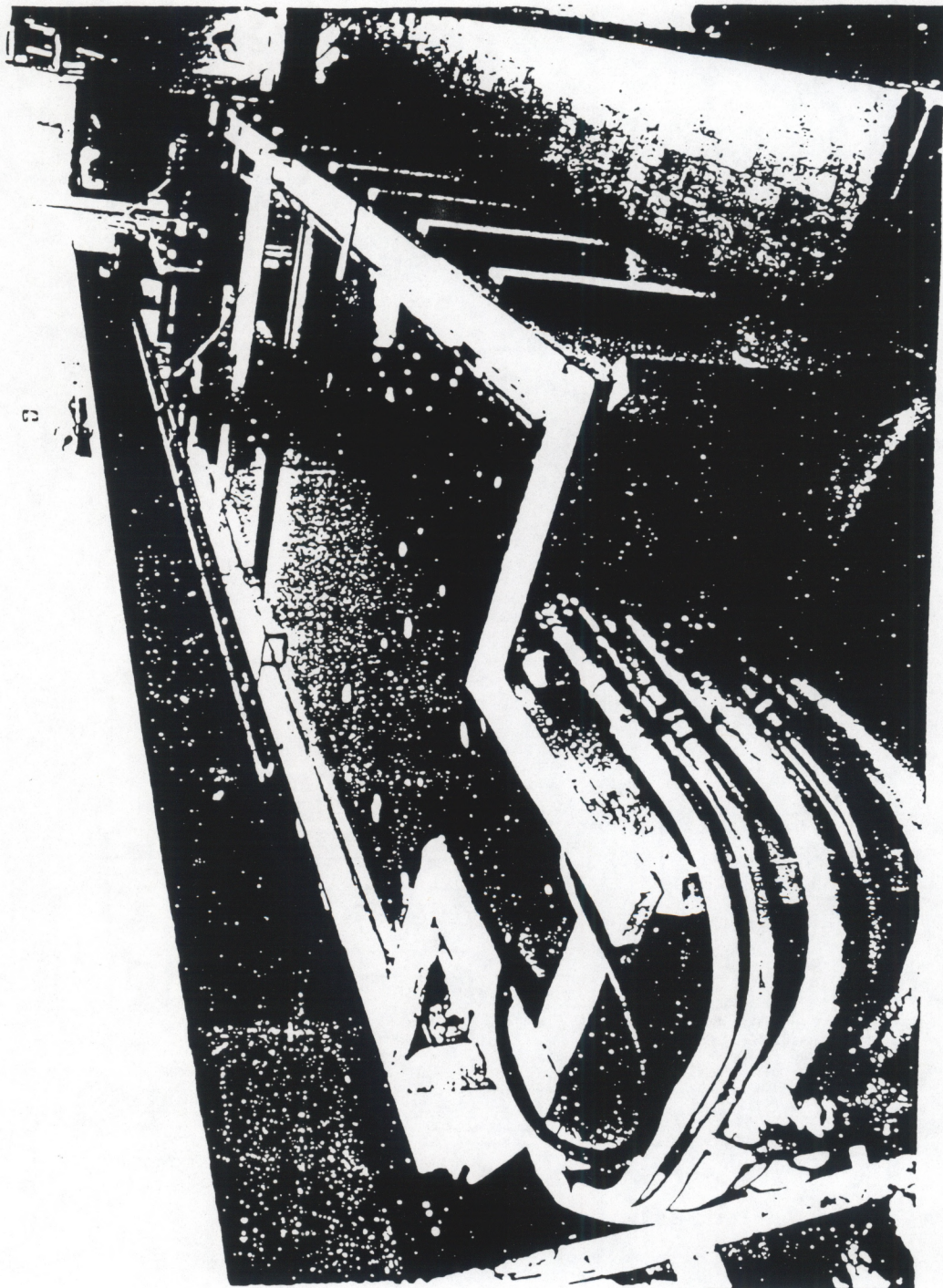


Fig. 18. General view of small thermostratified tank.

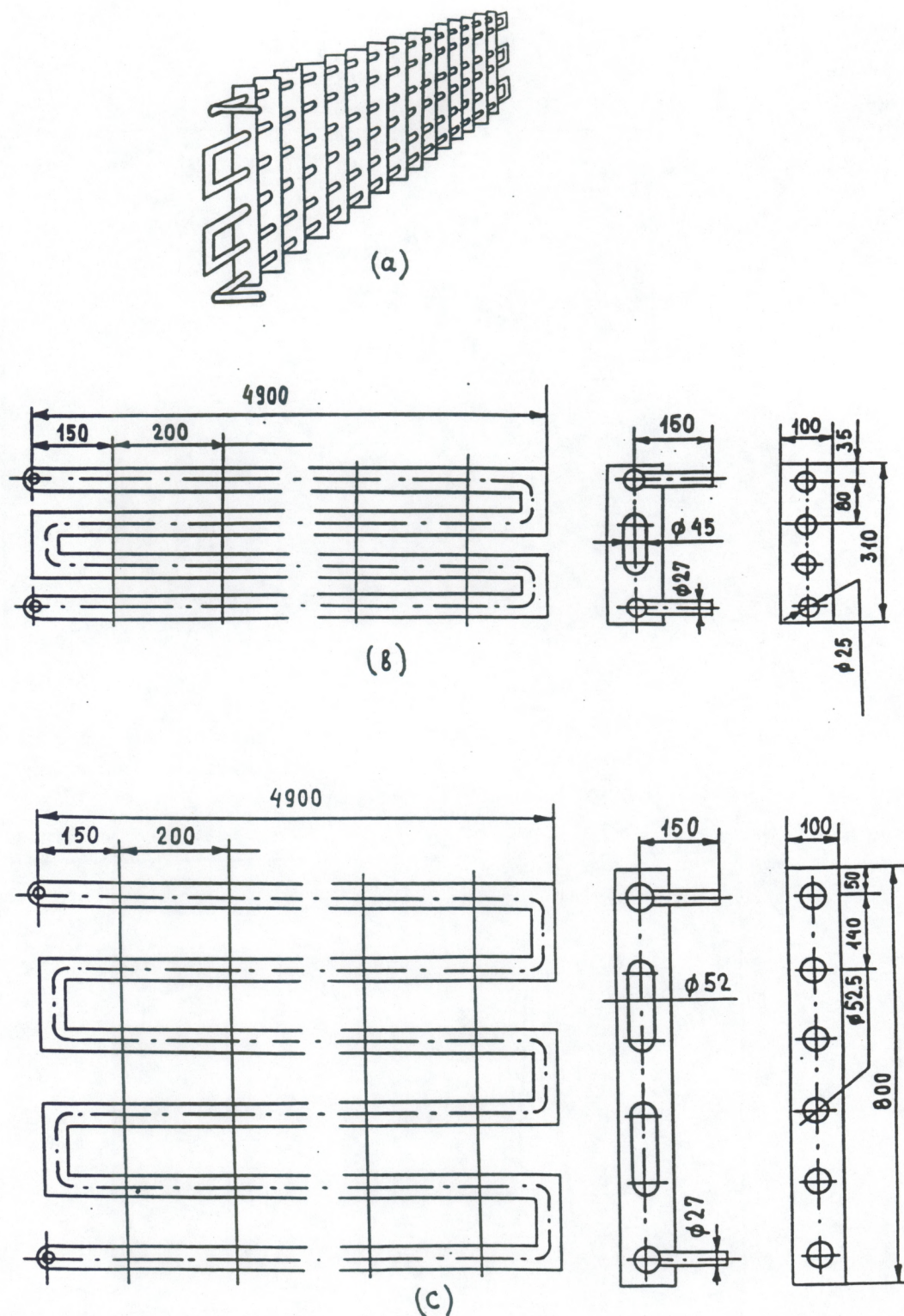


Fig. 19. The heat exchanger construction (2nd design): (a) general view; (b) upper heat exchanger; (c) lower heat exchanger. Dimensions are in millimeters.

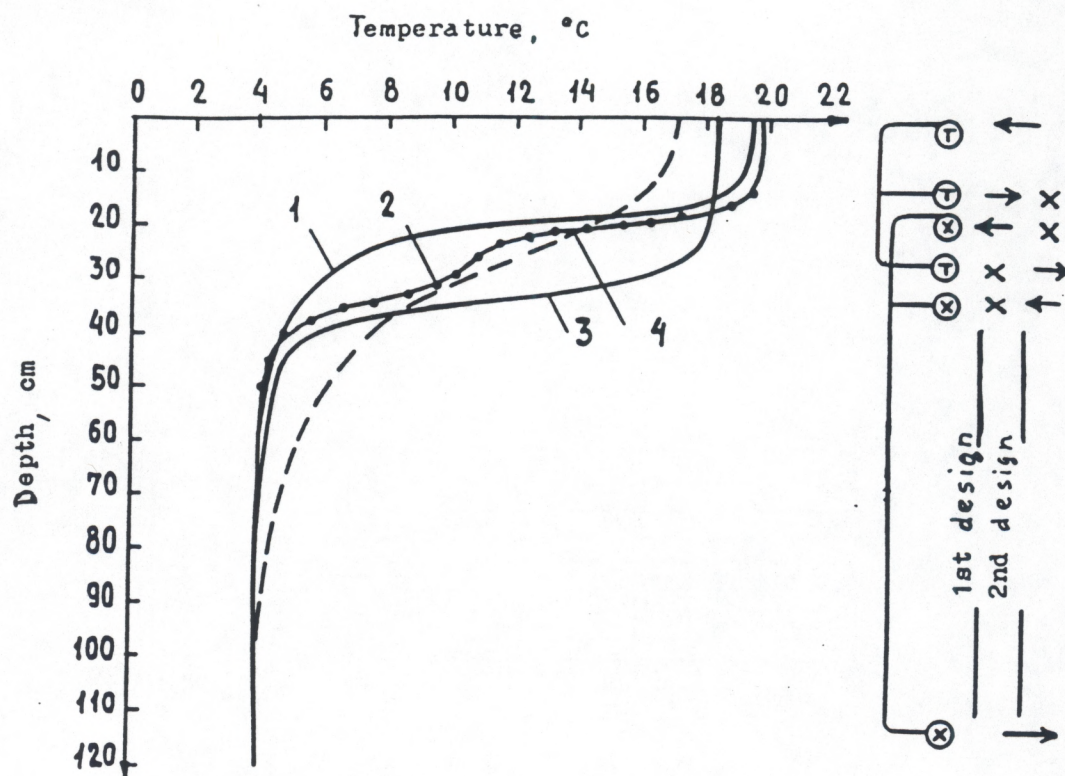


Fig. 20. Profiles of temperature stratification in the small tank: 1 - 1st design; 2 - 2nd design; 3 - 2nd model of heat exchanger; 4 - 18 h after refrigerator has turned off.

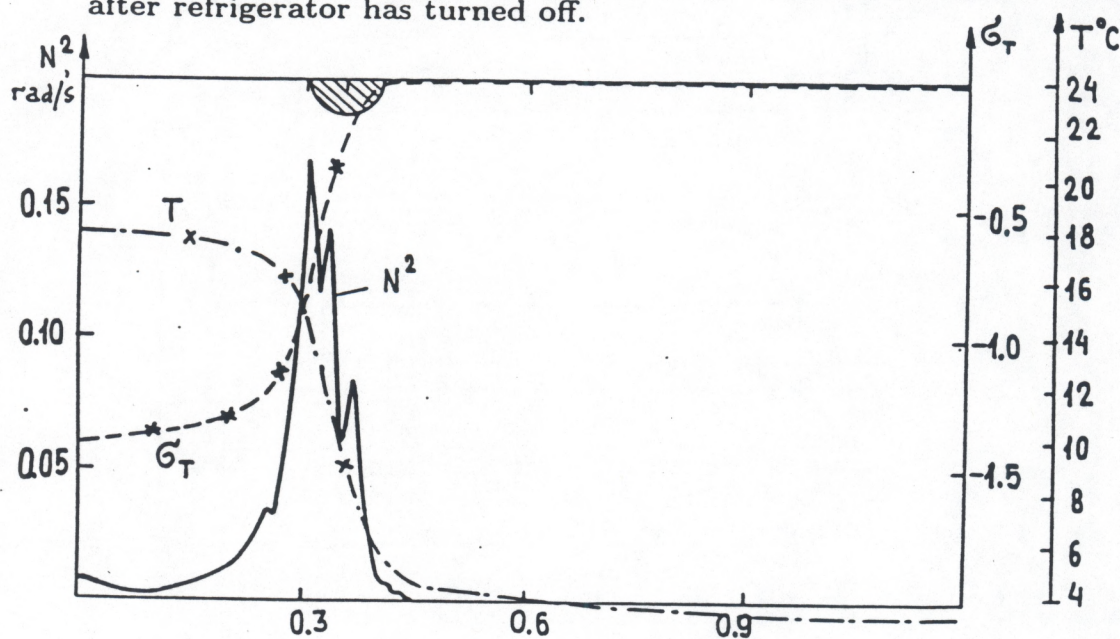


Fig. 21. Variations of temperature (T), relative density (σ_T), and squared Brunt - Vaisala frequency (N^2) vs depth provided by the 2nd design heat exchanger.

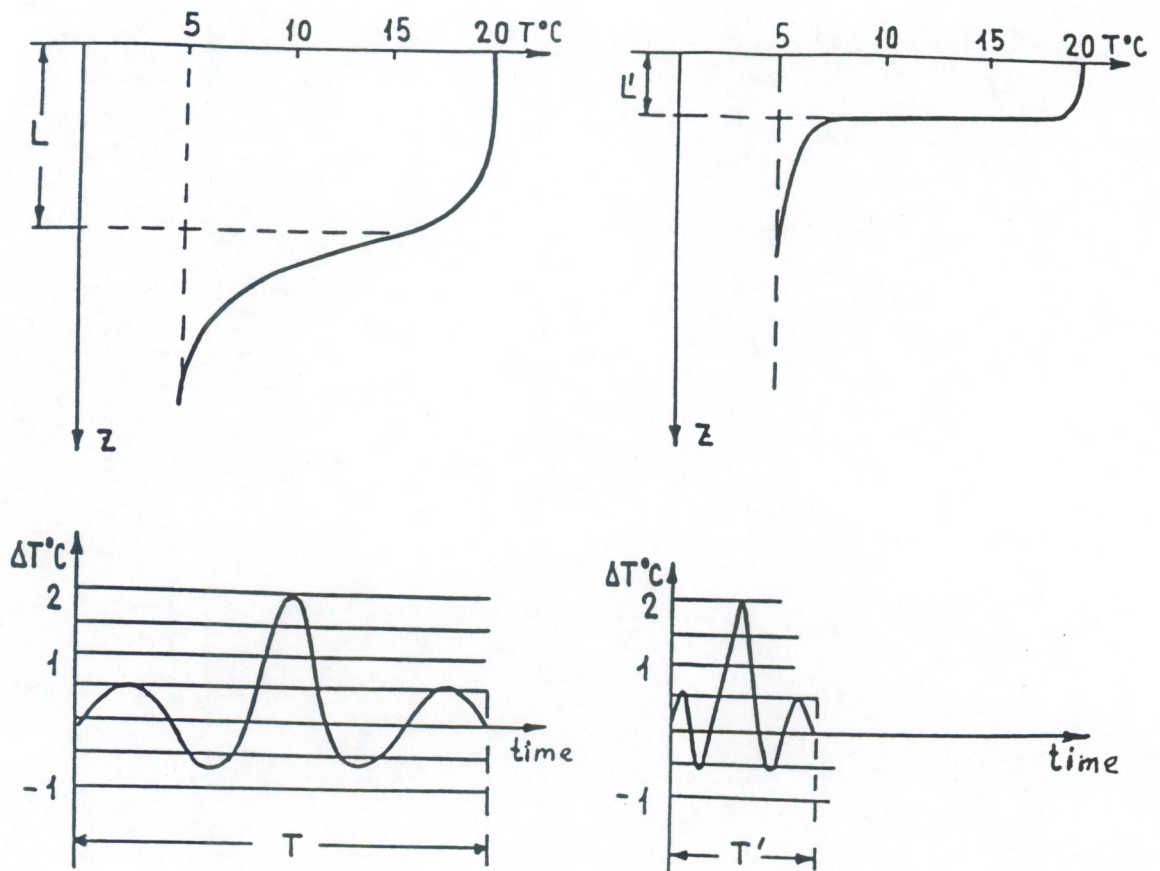
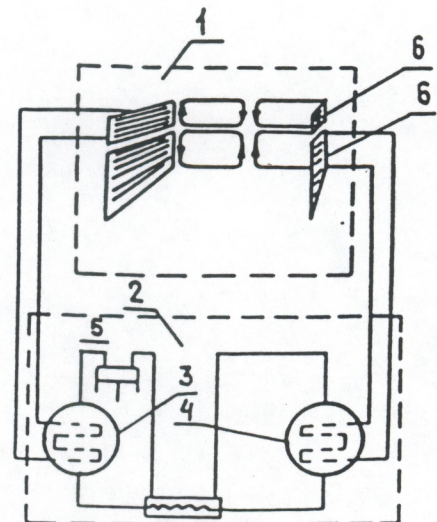


Fig. 22. Scale modeling of stratification ($L \rightarrow L'$) and of corresponding time scales ($T \rightarrow T'$).

Fig. 23. Schematic of devices to form stratification in the small tank:

- 1 - hydrochannel
- 2 - refrigerator
- 3 - condensor
- 4 - evaporator
- 5 - compressor
- 6 - heat exchangers.



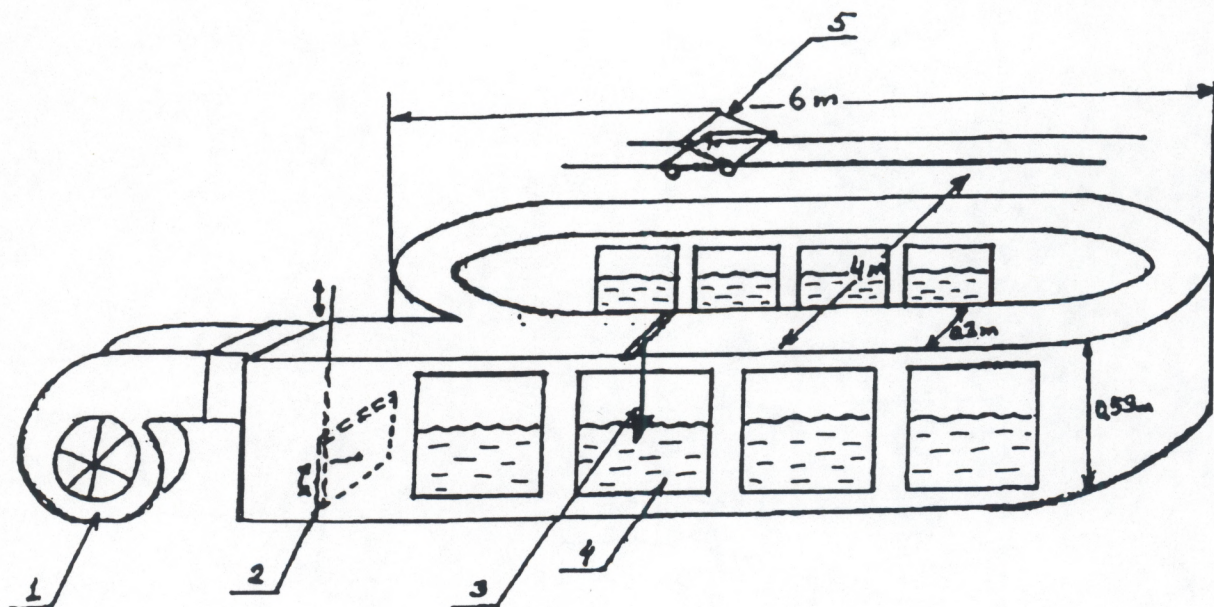


Fig. 24. Oval wind - wave tank:

- 1 - wind blower
- 2 - IW generator
- 3 - SW generator
- 4 - glass windows
- 5 - trolley.

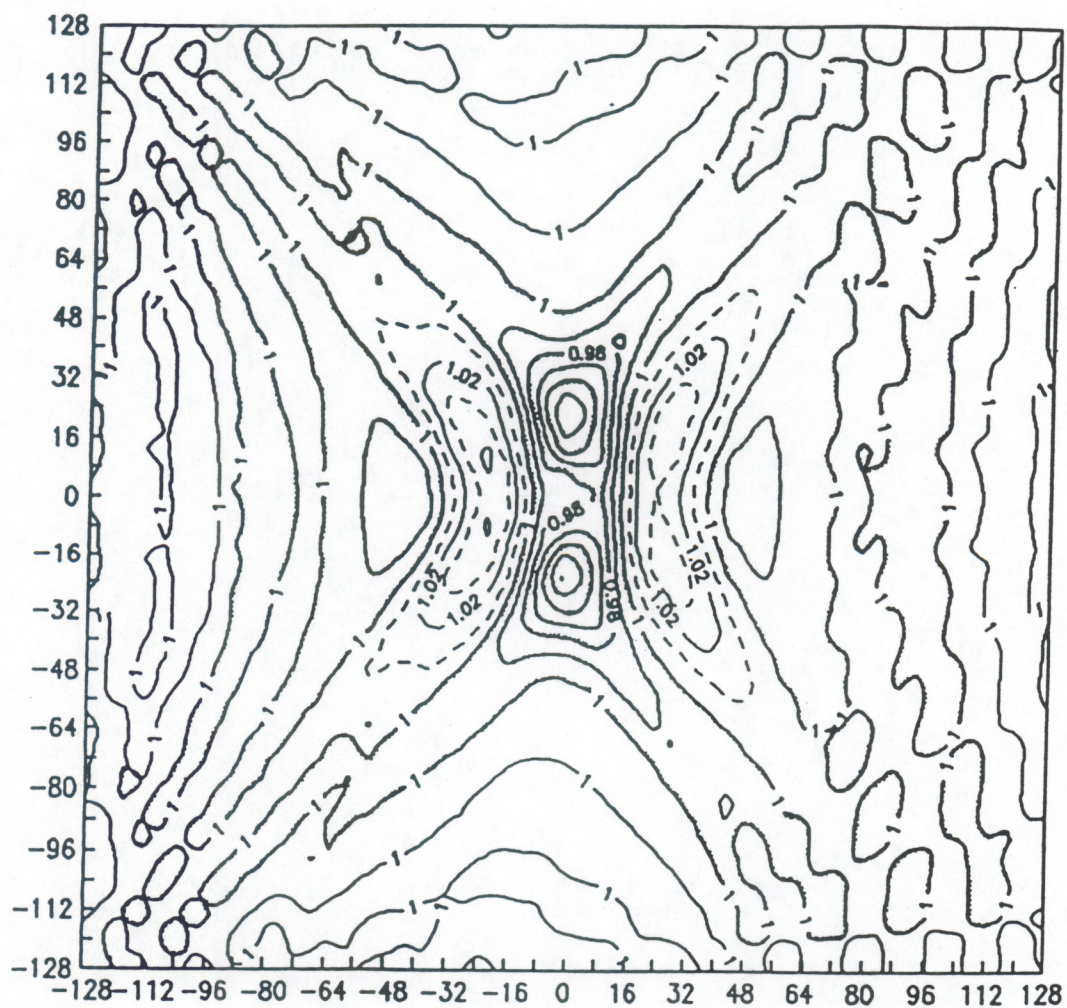
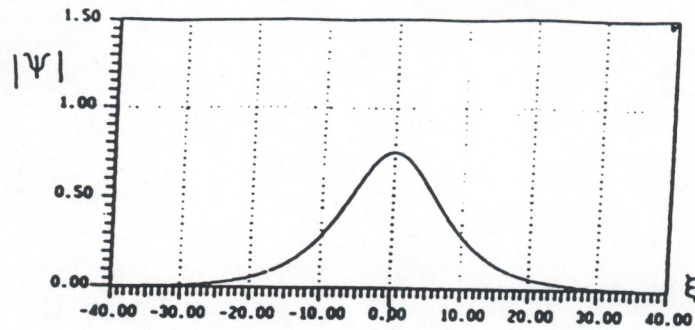
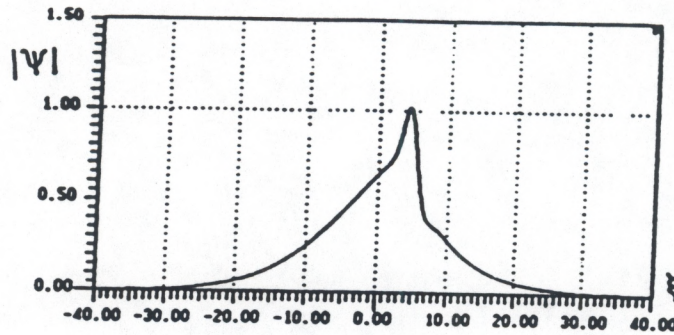


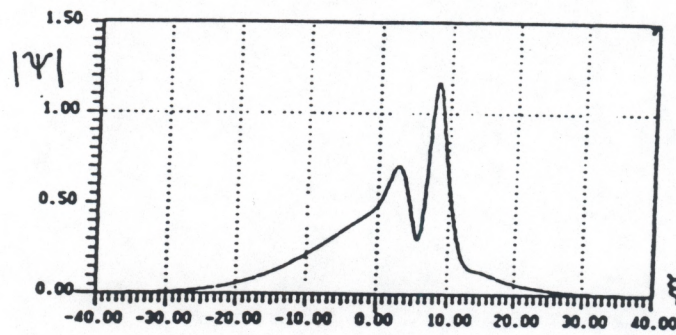
Fig. 25. Spatial distribution of the contrast function $|\alpha|^2(\hat{x}, \hat{y})$ for $\hat{k}_{x0}=1, \hat{k}_{y0}=0, c=2, \hat{h}=10, \hat{l}=600$.



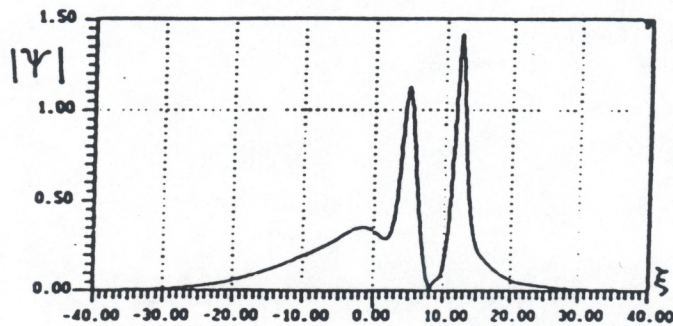
(a)



(b)



(c)



(d)

Fig. 26. Evolution of wave packet amplitude, $|\Psi|$, under the initial condition (12). Plots (a), (b), (c), and (d) correspond to the dimensionless moments $\tau = 0, 7, 14$, and 21 , respectively.

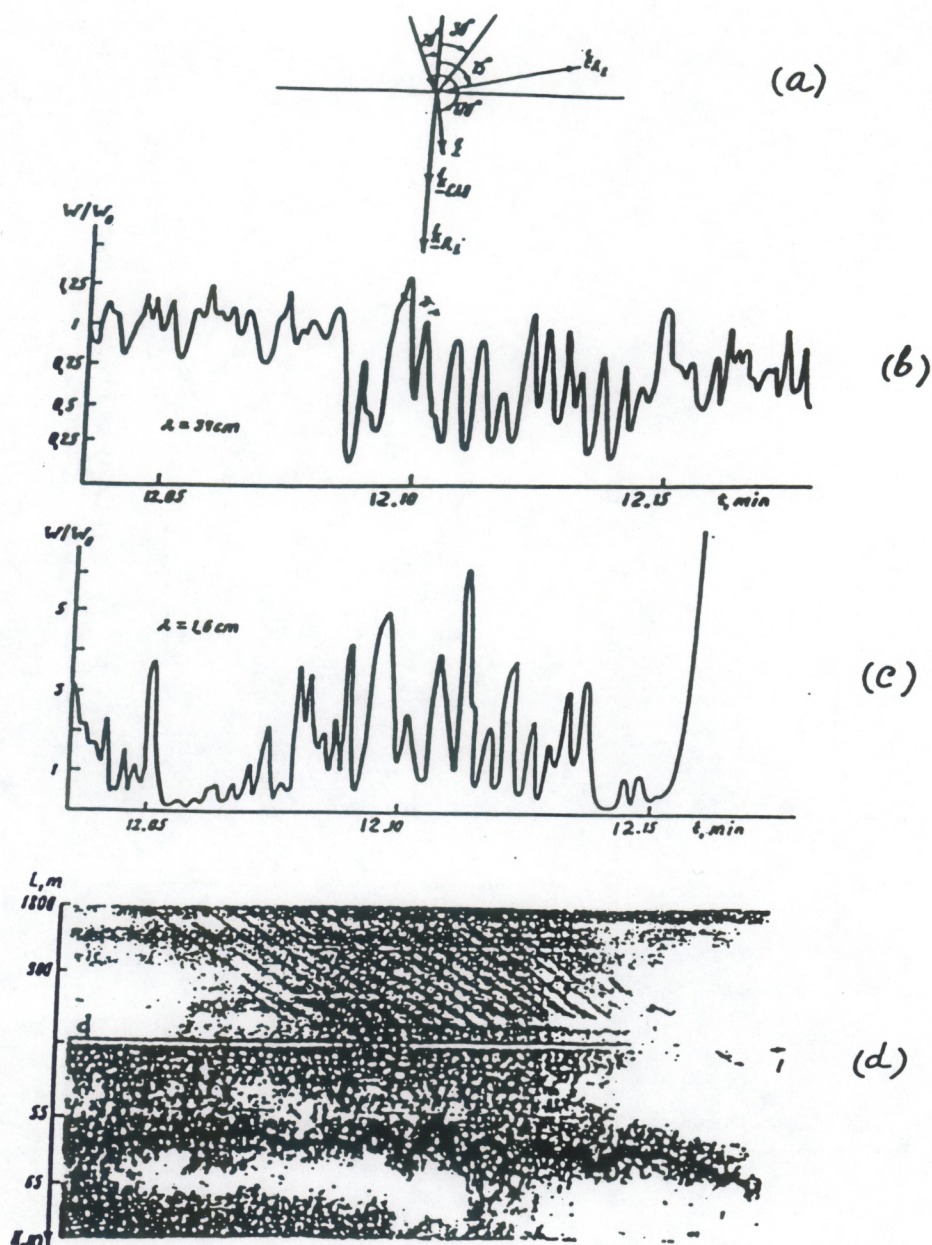


Fig. 27. Some results of the field experiment:

(a) main directions (ship velocity \vec{U}_s , wave vector of IWs, \vec{q} , and wave vectors of SWs, recorded by the spectrum analyzer, \vec{k}_{CAO} , by radar, \vec{k}_R , and \vec{k}_{R2} , and wind velocity \vec{U}_w ; (b) variations of spectral density of SWs with wave vector \vec{k}_{SAO} and wavelength $\lambda = 34$ cm normalized to its average value outside the region of IW train influence; (c) relative variation of spectral density of ripples of wavelength $\lambda = 1.6$ cm and wave vector \vec{k}_R ; (d) photograph made with radar set photorecorder (brightness is proportional to ripple spectral density variations); L is the distance from the ship; (e) record of ultrasonic sonar showing oscillations of sound scattering layers caused by IW train.

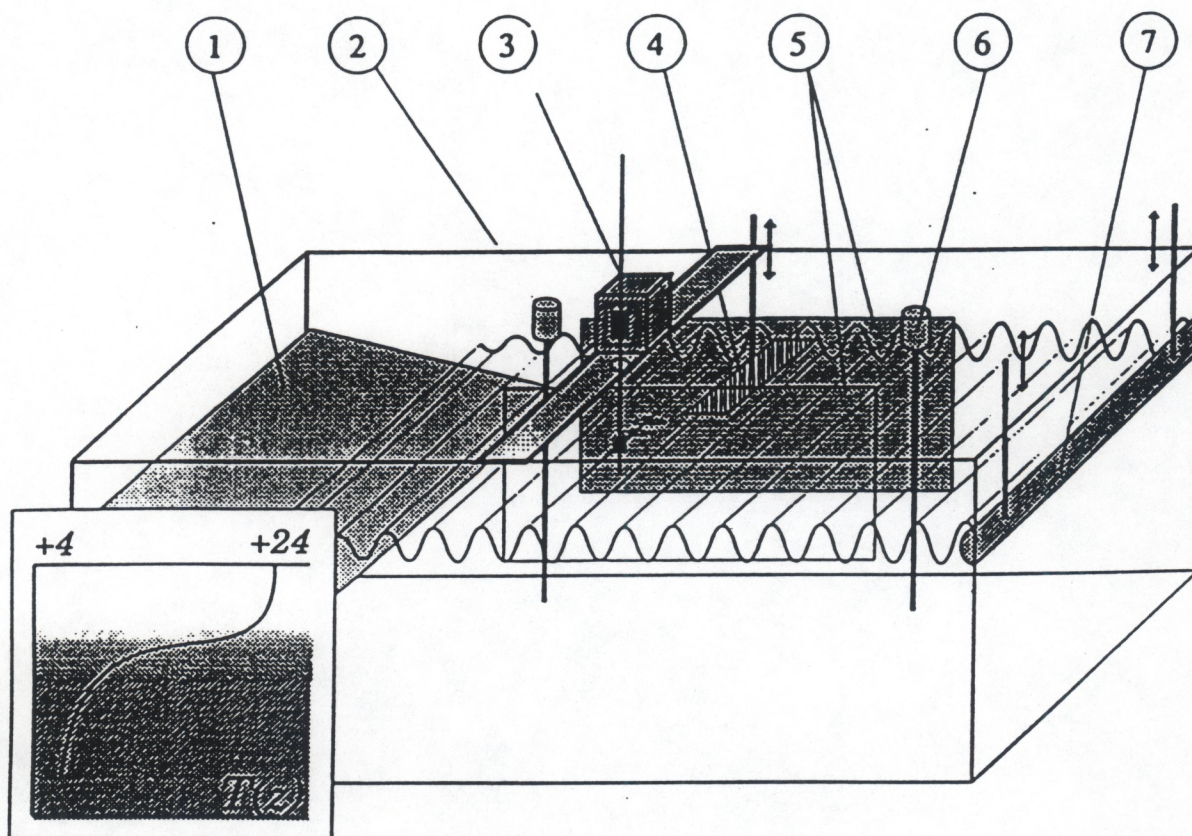


Fig. 28. The experimental setup for measurement of IW damping by turbulence: 1 - wave absorbed; 2 and 6 - wire temperature gauges; 3 - scanning tool with a thermistor and a hot - wire anemometer; 4 - perforated grid; 5 - vertical plexiglass walls; 7 - IW generator.

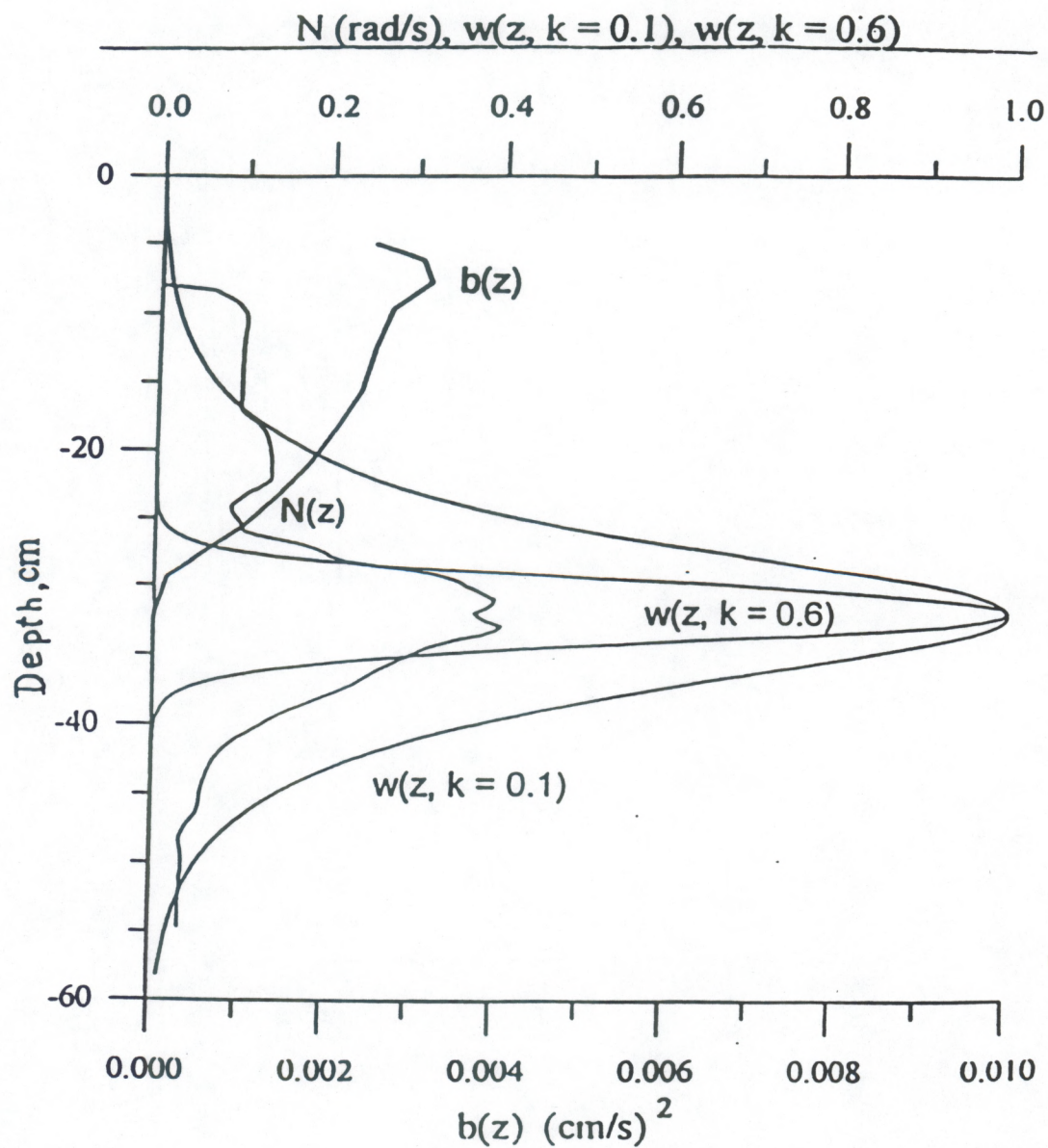


Fig. 29. Measured profiles of Brunt-Vaisala frequency N , turbulent energy b and calculated profiles of vertical velocity component w in the first IW mode for two horizontal wave numbers K .

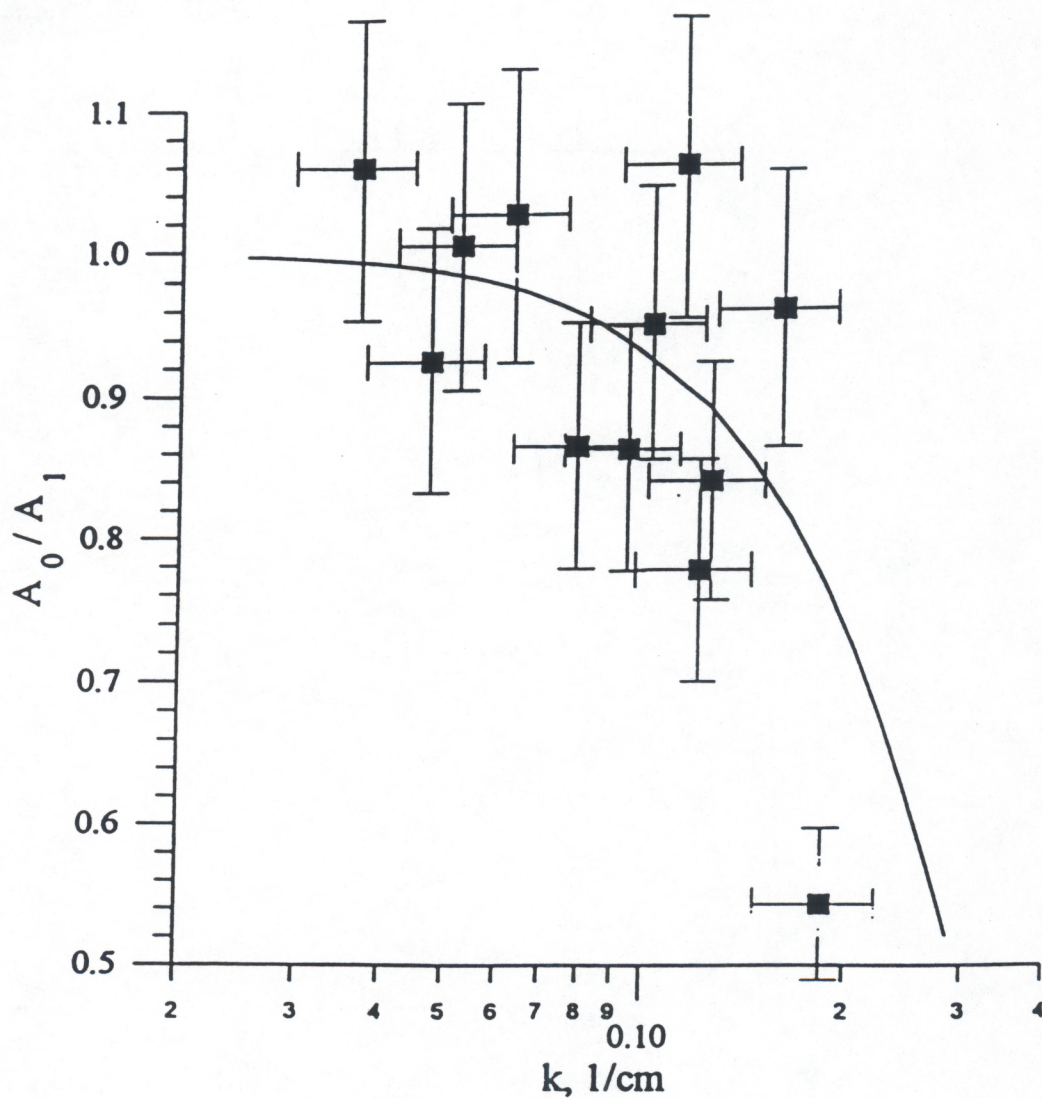


Fig. 30. IW damping (the ratio of IW amplitudes before and after the turbulent layer) as a function of the wave number. The grid is located 6 cm below the surface and driven with a frequency of 5 Hz. Solid line - theoretical calculation. Vertical lines mark the maximal possible experimental errors.

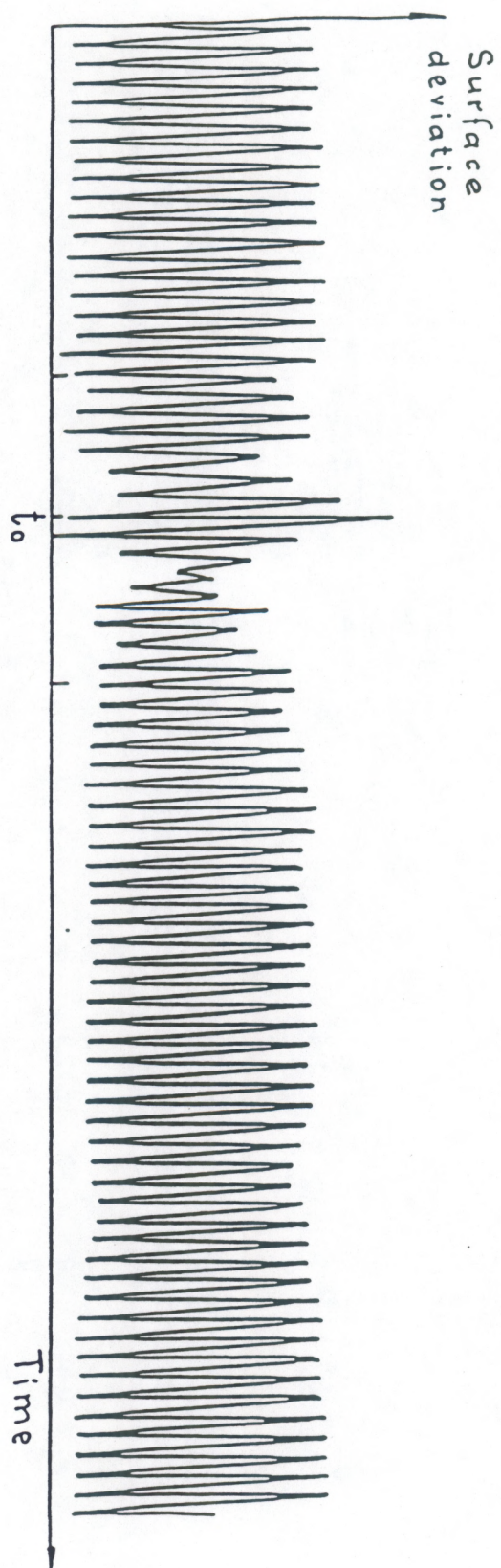


Fig. 31. Oscillations of water surface in time. t_0 is the moment of a sensor passage by the sphere.

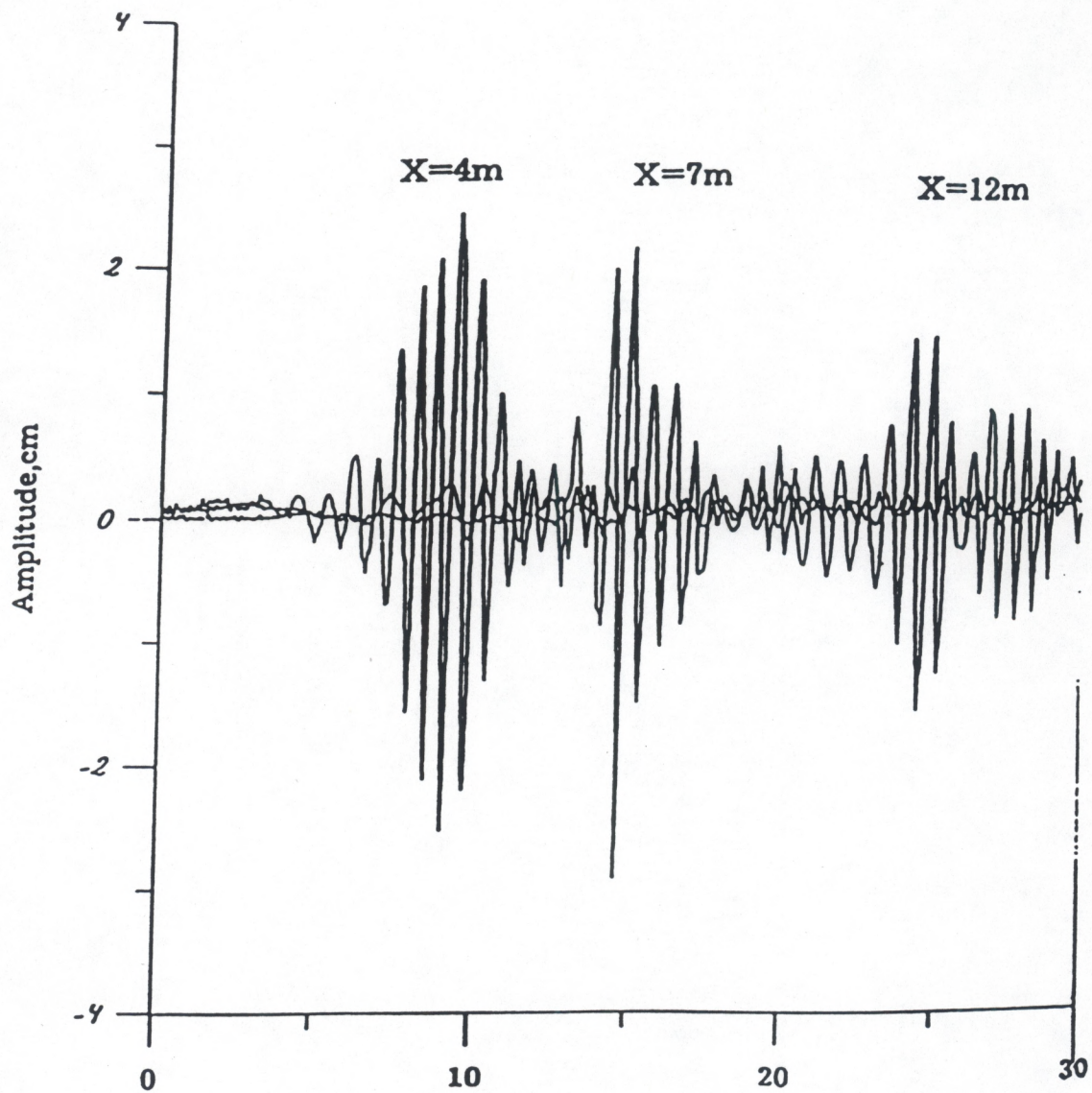


Fig. 32. Oscillograms of water - surface deviations a , in SW at distances $X = 4$ m (a) and 7 m (b) from the wave generator. The initial amplitude of the packet $a_0 = 3$ cm.

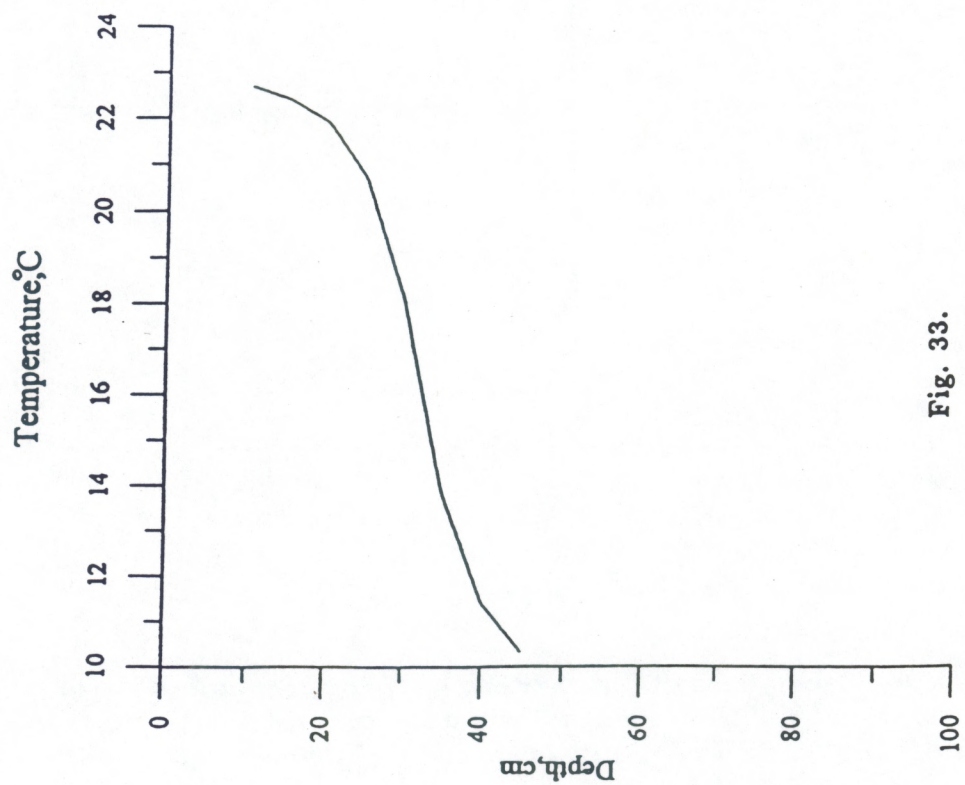


Fig. 33.

Water temperature T versus tank depth.

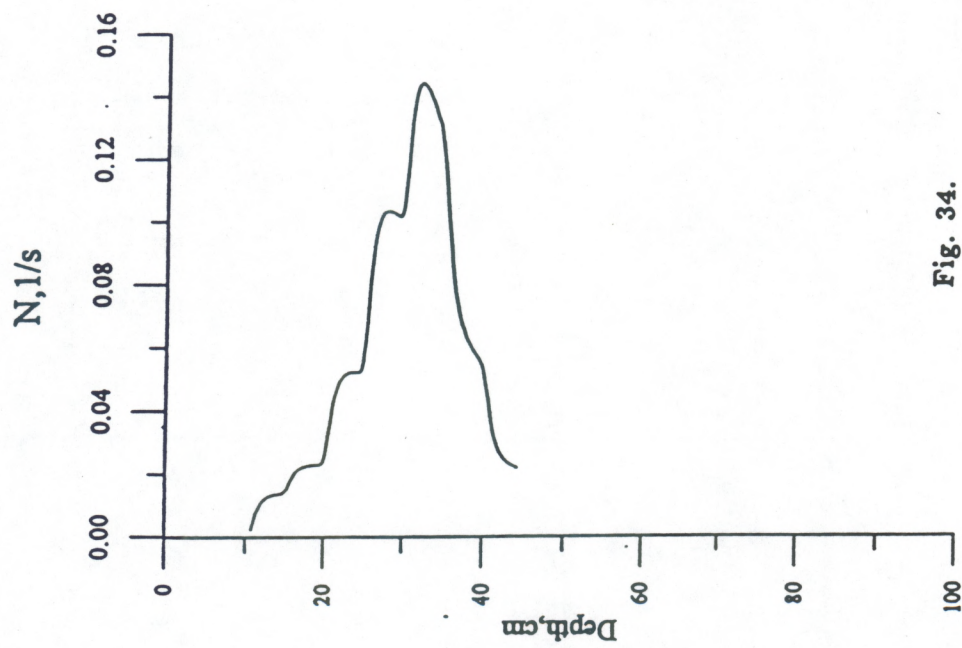


Fig. 34.

Water temperature gradient dT/dz versus tank depth.

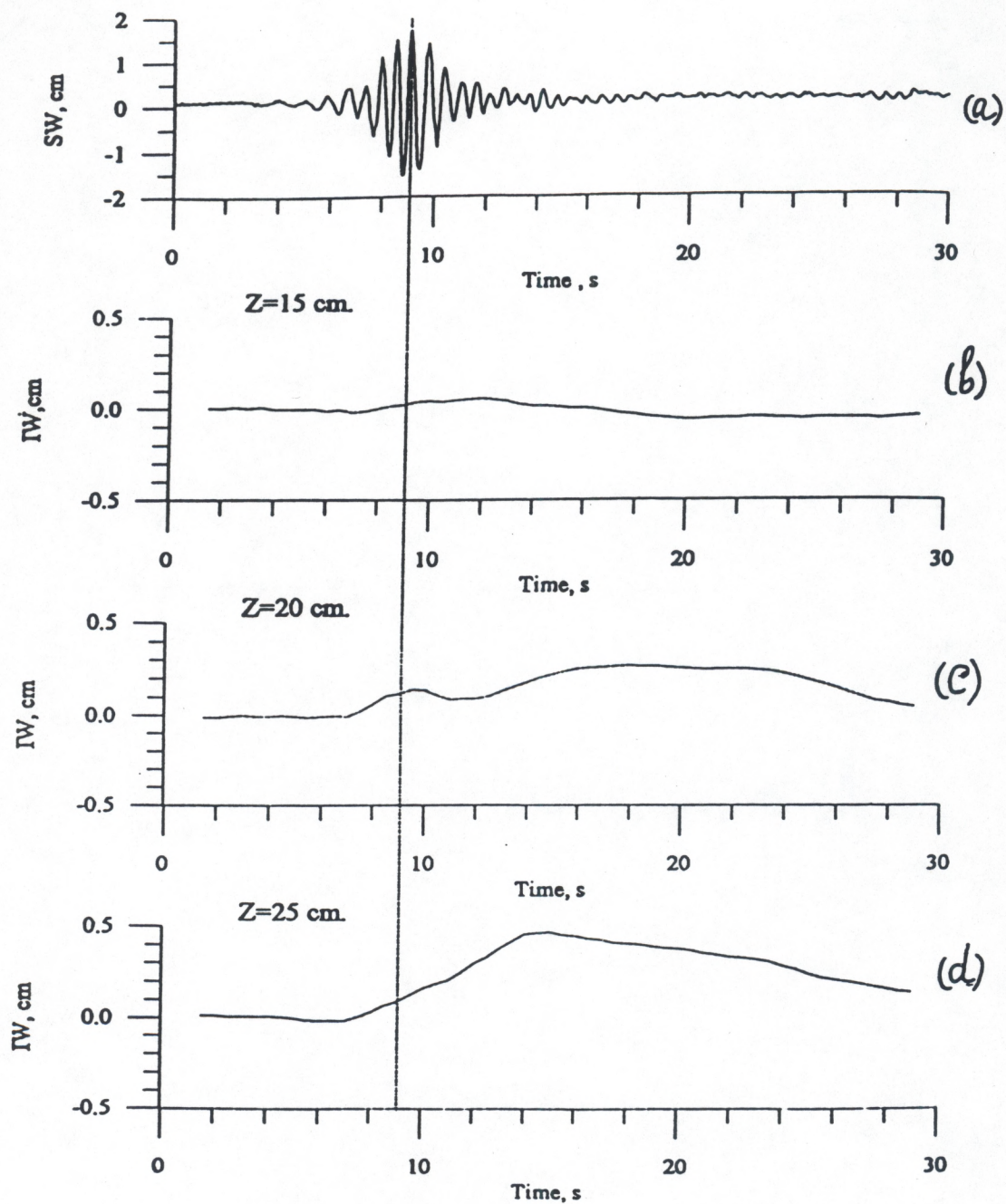


Fig. 35. Oscillations of fluid surface in SW, *a*, (a) and deviations of temperature ΔT from its equilibrium value at depths 15 cm (b), 20 cm (c) and 25 cm (d) at a distance of 4 m from wave generator.